



CrossMark

# Volatile Composition and Outgassing in C/2018 Y1 (Iwamoto): Extending Limits for High-resolution Infrared Cometary Spectroscopy between 2.8 and 5.0 $\mu\text{m}$

Michael A. DiSanti<sup>1,2,9</sup> , Boncho P. Bonev<sup>3,9</sup> , Neil Dello Russo<sup>4,9</sup> , Adam J. McKay<sup>1,3,9</sup> , Nathan X. Roth<sup>5,6,9</sup> ,  
Mohammad Saki<sup>7,9</sup> , Erika L. Gibb<sup>7,9</sup> , Ronald J. Vervack Jr.<sup>4,9</sup> , Younas Khan<sup>7,9</sup> , and Hideyo Kawakita<sup>8</sup>

<sup>1</sup> Solar System Exploration Division, Planetary Systems Laboratory Code 693, NASA-Goddard Space Flight Center, Greenbelt, MD, USA  
[michael.a.disanti@nasa.gov](mailto:michael.a.disanti@nasa.gov)

<sup>2</sup> Goddard Center for Astrobiology, NASA-Goddard Space Flight Center, Greenbelt, MD, USA

<sup>3</sup> Department of Physics, American University, Washington, DC, USA

<sup>4</sup> Johns Hopkins University Applied Physics Laboratory, Laurel, MD, USA

<sup>5</sup> Solar System Exploration Division, Astrochemistry Laboratory Code 691, NASA-Goddard Space Flight Center, Greenbelt, MD, USA

<sup>6</sup> Universities Space Research Association, Columbia, MD, USA

<sup>7</sup> Department of Physics and Astronomy, U. Missouri–St. Louis, St. Louis, MO, USA

<sup>8</sup> Koyoma Astronomical Observatory, Kyoto Sangyo University Motoyama, Kamingamo, Kita-ku, Kyoto 603-8555, Japan

Received 2021 February 24; revised 2021 May 28; accepted 2021 June 1; published 2021 November 9

## Abstract

We used the powerful high spectral resolution cross-dispersed facility spectrograph, iSHELL, at the NASA Infrared Telescope Facility (IRTF) to observe C/2018 Y1 (Iwamoto), a long-period comet from the Oort cloud. We report production rates for water and eight other parent molecules (native ices),  $\text{C}_2\text{H}_6$ , CO,  $\text{CH}_4$ ,  $\text{H}_2\text{CO}$ ,  $\text{CH}_3\text{OH}$ , HCN,  $\text{NH}_3$ , and  $\text{C}_2\text{H}_2$ , on three preperihelion UT dates, 2019 January 13 and (near perihelion) February 4–5. We present abundance ratios relative to both  $\text{C}_2\text{H}_6$  (a nonpolar molecule) and  $\text{H}_2\text{O}$  (a polar molecule), thereby providing a more complete picture of the parent volatile composition of C/2018 Y1 and potential associations of ices in its nucleus. Overall, the measured spatial distributions for polar molecules (in particular,  $\text{H}_2\text{O}$  and  $\text{CH}_3\text{OH}$ ) were broader, exhibiting more complex structure compared with nonpolar or weakly polar species ( $\text{CH}_4$ ,  $\text{C}_2\text{H}_6$ , and CO). Our January 13 results permitted quantitatively assessing the significant improvement in sensitivity delivered by iSHELL compared with previous capabilities at the IRTF. The efficient spectral coverage of iSHELL plus the favorable geocentric Doppler shift of C/2018 Y1 allowed for measuring  $>50\%$  of  $\text{CH}_4$   $\nu_3$ -band emission intensity on both January 13 and February 5. Compositionally, compared to their respective mean abundances among comets from the Oort cloud,  $\text{C}_2\text{H}_6$  and  $\text{CH}_3\text{OH}$  were enriched,  $\text{CH}_4$  and HCN were near normal, and all other species were depleted. The abundance ratio  $\text{CH}_3\text{OH}/\text{C}_2\text{H}_6$  was higher by  $45\% \pm 8\%$  on January 13 versus February 5, whereas  $\text{CH}_4/\text{C}_2\text{H}_6$  was unchanged within the uncertainty, suggesting nonhomogeneous composition among regions of the nucleus dominating activity on these dates.

*Unified Astronomy Thesaurus concepts:* Comet volatiles (2162); Comae (271); Solar system (1528); Small Solar System bodies (1469); Comets (280)

## 1. Background and Significance of This Study

The continually evolving taxonomy of ice abundances in comets tests conditions in the early solar system. As small bodies, comets lack gravitational heating and so retain a relatively preserved compositional record of icy solar system material dating to their formation (Bockelée-Morvan et al. 2004; Mumma & Charnley 2011). Unambiguous diversity in volatile (ice) composition among the population of comets was first observed through measurements of product species (radicals) at optical wavelengths in a sample now numbering well over 200 comets (A’Hearn et al. 1995; Fink 2009; Langland-Shula & Smith 2011; Cochran et al. 2012; Schleicher & Bair 2014). Although lagging optical studies in terms of numbers of comets measured, spectroscopic studies in IR and millimeter/submillimeter regimes have allowed for quantifying

constituent ices housed in cometary nuclei (commonly referred to as “native” ices). When sublimed through solar heating, these native ices release parent volatiles (molecules) into the coma. Measuring abundances for a suite of 10 or more distinct parent volatiles has become common in the infrared (specifically,  $\lambda \sim 2.8\text{--}5.0 \mu\text{m}$ ), with more numerous (including more complex) molecular species measured at millimeter/submillimeter wavelengths (Dello Russo et al. 2016; Bockelée-Morvan & Biver 2017 and references therein).

The number of comets for which parent volatiles have been characterized in the IR now exceeds 40, and in terms of their abundance ratios relative to  $\text{H}_2\text{O}$  (the most abundant ice in comets), trends continue to be established (and augmented) according to whether a given volatile is enriched, consistent with, or depleted relative to its average abundance measured among comets. Each new comet measured has the potential of contributing significantly to this evolving taxonomy of ice compositions in cometary nuclei.

The new generation of powerful high-resolution ( $R \equiv \lambda/\Delta\lambda > 2 \times 10^4$ ), cross-dispersed infrared spectrographs operating in the  $1\text{--}5 \mu\text{m}$  spectral region has enabled advancements in studies of sublimed native ices in significant ways. Current state-of-the-art instruments include the recently upgraded Keck/NIRSPEC (Martin et al. 2018) and Infrared

<sup>9</sup> Visiting astronomer at the Infrared Telescope Facility, which is operated by the University of Hawaii under National Aeronautics and Space Administration contract NNH14CK55B.



Original content from this work may be used under the terms of the [Creative Commons Attribution 4.0 licence](https://creativecommons.org/licenses/by/4.0/). Any further distribution of this work must maintain attribution to the author(s) and the title of the work, journal citation and DOI.

Telescope Facility (IRTF) iSHELL (Rayner et al. 2016), which is used for the study presented here. Both instruments incorporate modern  $2048 \times 2048$  pixel detector arrays having very low dark current and read noise.

Compared to its predecessor and legacy instrument of this type, CSHELL (Tokunaga et al. 1990), iSHELL features higher resolving power ( $R \cong 4 \times 10^4$ , when matched to the nominal seeing point-spread function, PSF,  $\sim 07$ ) and provides significantly improved sensitivity and spectral coverage for a given instrument setting. Examples showing the layout of iSHELL orders for specific instrument settings can be found in the literature (DiSanti et al. 2017; Faggi et al. 2018; for the updated iSHELL manual, see <http://irtfweb.ifa.hawaii.edu/~ishell/>).

In this paper, we present results from preperihelion iSHELL observations of Comet C/2018 Y1 (Iwamoto; hereafter C/2018 Y1), a long-period ( $\sim 1730$  yr), moderately bright comet from the Oort cloud, a dynamical population frequently referred to as “nearly isotropic comets” or “Oort cloud comets” (OCCs). It was discovered on 2018 December 18 and reached perihelion on UT 2019 February 7 at heliocentric distance  $R_h = 1.287$  au. We report production rates for  $C_2H_6$  and  $H_2O$  on multiple dates and production rates and abundance ratios relative to both  $C_2H_6$  and  $H_2O$  for these and seven additional parent molecules (CO,  $CH_4$ ,  $H_2CO$ ,  $CH_3OH$ ,  $C_2H_2$ , HCN, and  $NH_3$ ). The capabilities of iSHELL have extended our ability to assess spatial distributions of emissions to fainter comets and, coupled with the highly favorable observational circumstances for C/2018 Y1, have permitted simultaneous measurement of more than half the total  $CH_4$   $\nu_3$ -band intensity.

## 2. Observations of C/2018 Y1 with iSHELL

We obtained long-slit spectra of C/2018 Y1 at the IRTF on the summit of Maunakea, Hawaii, on three preperihelion dates. This included “test” integrations on UT 2019 January 13, and, based on clear molecular detections seen in these, we conducted follow-up observations near perihelion on February 4–5, by which time the comet had brightened significantly. These three dates (plus February 7, which was weathered out) were assigned in support of the worldwide observing campaign on Jupiter-family comet (JFC) 46P/Wirtanen, which was setting as C/2018 Y1 fortuitously became available for the final 2–3 hr of the night. This allowed us to obtain high-quality spectra of C/2018 Y1 on multiple dates, only  $\sim 1$ –1.5 months following its discovery.

Our study spanned a limited range in  $R_h$  (1.34–1.29 au; Table 1); however, the geocentric distance ( $\Delta$ ) of C/2018 Y1 decreased by a factor of  $\sim 2.5$  between our January and February observations. This combined change in observing circumstances increased the brightness of the spectral lines by a factor of approximately 3. The geocentric Doppler shift ( $\Delta_{dot}$ ) was highly favorable throughout this period, permitting robust measures of CO and (especially)  $CH_4$ .

Spectra were obtained using our standard ABBA sequence of telescope nodding, with both A and B beams in the slit, positioned symmetrically with respect to its midpoint and spatially separated by half its length (75). For all observations, we oriented the slit along the projected Sun–comet direction, which allowed for comparing the release of material (molecules and dust) into sunward- versus antisunward-facing hemispheres. In addition to C/2018 Y1, to establish absolute flux calibration, we obtained spectra of infrared flux standards in all comet settings using a

wider ( $4''$  wide) slit to minimize the loss of signal and thereby achieve a true measure of stellar continuum flux.

Due to our emphasis on Comet Wirtanen, we obtained spectra of C/2018 Y1 on UT January 13 only in the Lp1 setting. Compared with other settings, Lp1 encompasses more intrinsically strong emission from multiple organic molecules (in particular,  $CH_4$ ,  $C_2H_6$ ,  $CH_3OH$ , and  $H_2CO$ ). Accordingly, this setting was chosen to test cometary activity and thereby better plan for subsequent studies in February, by which time Wirtanen had faded considerably while C/2018 Y1 had brightened.

## 3. Spectral Analysis

We processed individual spatial-spectral orders as detailed in the literature (DiSanti et al. 2006; Villanueva et al. 2009; Radeva et al. 2010; DiSanti et al. 2017). For each order, this resulted in a flat-fielded, cleaned, and rectified two-dimensional (spatial-spectral) frame, each row of which corresponded to a unique spatial position along the slit and each column to a unique wavelength.

We produced line spectra from the processed comet frames by summing signal over 15 rows centered on the peak emission intensity. These represent signal contained within a rectangular aperture of size  $075 \times 25$ , which we refer to as “nucleus-centered” spectra. Examples are shown in Figures 1–3. The upper black lines in Figures 1(a) and (b), 2, and 3(a)–(c) represent observed comet spectra. The modeled continuum (overlaid gold lines in Figures 1(a) and (b), 2 and 3(a) and (c)) representing the best-fit telluric transmittance function was produced using the GENLN3 line-by-line radiative transfer code (Collins et al. 2006) including updated line lists and strengths (Villanueva et al. 2011a) and was validated using the Planetary Spectrum Generator (<https://psg.gsfc.nasa.gov/>; Villanueva et al. 2008).

The transmittance model was calculated at very high spectral resolving power ( $R = 1.5 \times 10^6$ ; referred to as the “fully resolved” or “monochromatic” transmittance), convolved to the resolution of the comet spectra ( $R \cong 4 \times 10^4$ ), and then scaled to the observed continuum level. Below this are molecular fluorescence models at the most likely rotational temperature, as measured from our January and February nucleus-centered comet spectra (see Table 2 and related discussion in Section 3.1). Models are color-coded and labeled by molecule and (in Figure 1) rovibrational band. To more clearly reveal weaker emissions, fluorescence models are scaled vertically where indicated. To more clearly reveal weaker emissions, Figures 1(c) and (d) and 3(b) show continuum-subtracted spectra expanded over shaded regions as indicated the figures.

Nucleus-centered spectra from multiple overlapping Lp1 orders are shown in Figure 1, with the spectral coverage of each denoted by horizontal bars above the observed comet spectrum. This spectral interval comprises the brightest portion of the “cometary organics region” spanning  $\sim 3.2$ – $3.6 \mu m$ , first identified during the Vega and Giotto flybys of comet 1P/Halley (Moroz et al. 1987; Combes et al. 1988; Langevin et al. 1988), with constituent species studied in detail through in situ measurements of JFC 67P/Churyumov–Gerasimenko over the course of the Rosetta mission (e.g., see Morse & Chan 2019 and references therein).

Fluorescence models were shifted in frequency according to the geocentric velocity of C/2018 Y1 ( $\Delta_{dot}$  in Table 1) and multiplied by the monochromatic transmittance at each Doppler-shifted line frequency. Models were then convolved to the spectral resolution of the comet spectra and matched to the observed cometary line intensity in excess of the continuum.

**Table 1**  
Log of IR Spectral Observations of C/2018 Y1 (Iwamoto)<sup>a</sup>

2019 UT Date	Setting ID/ Order <sup>b</sup>	$\nu^b$ ( $\text{cm}^{-1}$ )	UT Start–End	$R_h$ (au)	$\Delta$ (au)	$\Delta_{\text{dot}}$ ( $\text{km s}^{-1}$ )	Molecule(s) <sup>b</sup>	$T_{\text{int}}^c$ (min)	Slit PA (deg) <sup>d</sup>	$\beta^e$ (deg)
Jan 13	Lp1		14:23–15:30	1.3384	1.1725	–58.93		59.77	288	46
	o158	3062.8–3037.9					CH <sub>4</sub> , OH*			
	o157	3043.5–3019.0					CH <sub>4</sub> , OH*			
	o156	3024.4–2999.9					CH <sub>4</sub>			
	o155	3005.0–2980.7					C <sub>2</sub> H <sub>6</sub> , CH <sub>3</sub> OH, CH <sub>4</sub> , OH*			
	o154	2985.8–2961.5					C <sub>2</sub> H <sub>6</sub>			
	o147	2851.0–2827.8					CH <sub>3</sub> OH, OH*			
	o144	2793.1–2770.4					H <sub>2</sub> CO, OH*			
Feb 4	M2		14:00–14:51	1.2875	0.440 0	–48.21		38.92	296	39
	o111	2159.6–2141.5					CO, H <sub>2</sub> O			
	o110	2140.2–2122.2								
Feb 5	Lcust		11:44–13:24	1.2872	0.4150	–45.31		91.65	296	37
	o182	3523.0–3495.2					H <sub>2</sub> O, OH*			
	o179	3465.7–3437.8					H <sub>2</sub> O, OH*			
	o175	3388.9–3361.9					H <sub>2</sub> O, OH*			
	o172	3331.5–3304.6					HCN, C <sub>2</sub> H <sub>2</sub> , NH <sub>3</sub> , H <sub>2</sub> O			
	o171	3312.2–3285.6					HCN, C <sub>2</sub> H <sub>2</sub> , NH <sub>3</sub> , H <sub>2</sub> O			
	o170	3293.1–3266.6					HCN, C <sub>2</sub> H <sub>2</sub> , NH <sub>3</sub> , H <sub>2</sub> O			
	Lp1		13:43–14:59	1.2872	0.4131	–45.06		63.76	296	36
	o159 <sup>f</sup>	3068.6–3057.0					CH <sub>4</sub>			
	o158	3062.8–3037.9					CH <sub>4</sub> , OH*			
	o157	3043.5–3019.0					CH <sub>4</sub> , OH*			
	o156	3024.4–2999.9					CH <sub>4</sub>			
	o155	3005.0–2980.7					C <sub>2</sub> H <sub>6</sub> , CH <sub>3</sub> OH, CH <sub>4</sub> , OH*			
	o154	2985.8–2961.5					C <sub>2</sub> H <sub>6</sub>			
	o147	2851.0–2827.8					CH <sub>3</sub> OH, OH*			
	o144	2793.1–2770.4					H <sub>2</sub> CO, OH*			

**Notes.**

<sup>a</sup> The slit dimensions used for C/2018 Y1 were  $0''.75$  (6 spectral pixels)  $\times$   $15''$  on all dates. An early-type infrared flux standard star was observed in each setting on each date using a  $4'' \times 15''$  slit. January 13: BS4905 (spectral type = A0, L-magnitude = 1.75); February 4 and 5: BS4357 (spectral type = A4, L- (and M-) magnitude = 2.3).

<sup>b</sup> The iSHELL setting and orders analyzed, approximate frequency range covered within each order, and species targeted.

<sup>c</sup> Total on-source integration times by setting.

<sup>d</sup> Slit position angle on the sky, measured clockwise from north as usual. On all dates, this corresponded to the extended heliocentric radius vector (i.e., the projected Sun–comet direction) for C/2018 Y1.

<sup>e</sup> Denotes solar phase angle (Sun–comet–observer), as illustrated in the schematics of Figure 7.

<sup>f</sup> Order 159 was cut off at the short-wavelength end of the iSHELL Lp1 setting on February 5 (Figure 1(b)), and thus its frequency range is less than indicated for other orders.

The bottom line in each panel of Figures 1(a) and (b) (labeled “Residuals”) represents the observed minus total modeled spectrum (continuum plus molecular emissions). The cometary residuals fall

largely within the  $\pm 1\sigma$  stochastic noise envelope (magenta lines); note the larger noise in regions of sky-line emission, most pronounced for the CH<sub>4</sub>  $\nu_3$  Q branch near  $3015 \text{ cm}^{-1}$ .

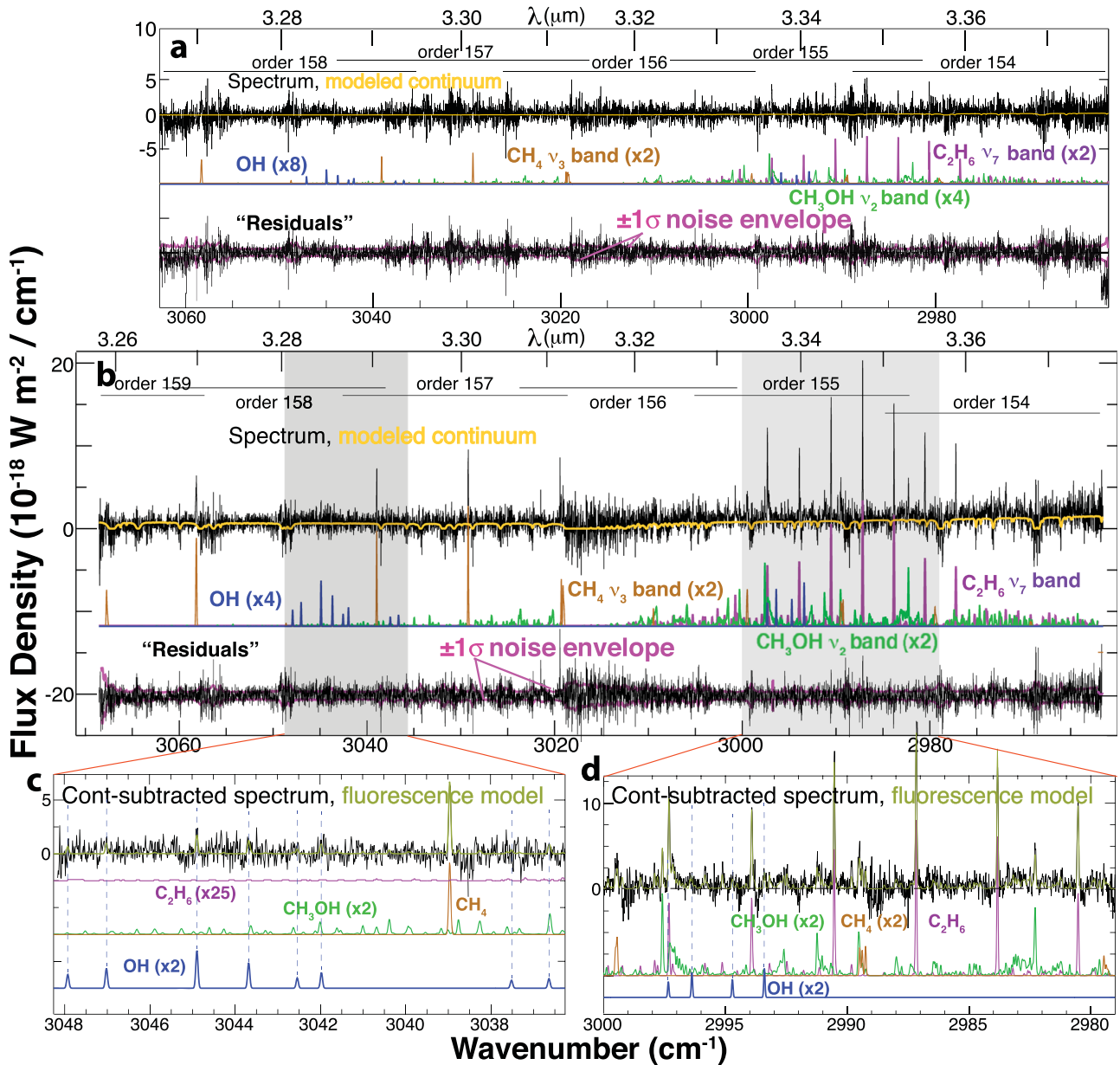


**Figure 1.** Nucleus-centered spectra ( $R \cong 4 \times 10^4$ ) of C/2018 Y1 obtained with iSHELL in the Lp1 setting and acquired on UT (a) January 13 and (b) February 5, both representing approximately 1 hr on source (Table 1). Echelle orders are labeled, and fluorescence models are color-coded by molecule and rovibrational band. In each panel, the bottom spectrum (labeled “Residuals”) represents the total modeled spectrum (volatiles + dust continuum) subtracted from the extracted spectrum. Note that the model for  $\text{CH}_3\text{OH}$  is scaled by a factor of 2 relative to that for  $\text{C}_2\text{H}_6$ ; see Section 4.4 for a compositional comparison. Panels (c) and (d) show expanded spectral regions from panel (b), more clearly revealing weaker emissions (in particular,  $\text{OH}^*$ ).

Signal was combined from overlapping spectral regions in adjacent orders. This is reflected in commensurately lower noise (by a factor of approximately  $1/\sqrt{2}$  for the approximately 20% of spectral channels in Figure 1 representing regions of order overlap, compared with channels containing signal from a single order alone. Figure 1 demonstrates our ability to quantitatively characterize emissions throughout this spectral region and also illustrates the pronounced increase in cometary line brightness and thus signal-to-noise ratio (S/N) over the approximately 3 week interval of January 13–February 5. In Section 4.1, we provide a quantitative assessment of recent advances in sensitivity afforded by iSHELL, including our ability with iSHELL to obtain valuable spatial information in considerably fainter comets than was previously possible at the

IRTF, using our January 13 observations of C/2018 Y1 as an example.

### 3.1. Rotational Temperatures

Individual line  $g$  factors depend on rotational temperature ( $T_{\text{rot}}$ ), representing the population distribution among rotational levels for specific molecules. A reliable value for  $T_{\text{rot}}$  can be established by measuring lines that sample a range of rotational energies. At the optimal (i.e., best-fit)  $T_{\text{rot}}$ , within the uncertainty, all lines provide a common production rate or, equivalently, a common molecular column density (Section 3.2). This was performed for multiple parent volatiles targeted in C/2018 Y1 (Table 2), for example, based on a linear least-squares fit, as first demonstrated through measurement of  $\text{H}_2\text{O}$  lines in comet 153P/Ikeya–Zhang



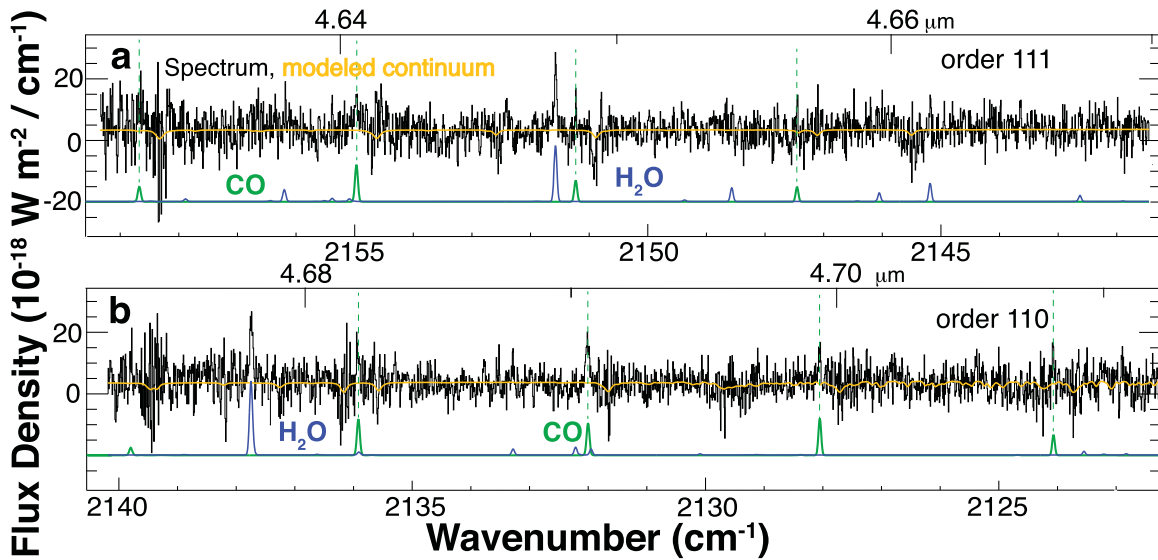


**Figure 2.** Nucleus-centered spectra of C/2018 Y1 from the M2 setting on February 4, showing comeasured emission lines of CO (marked with dashed green vertical lines) and H<sub>2</sub>O. The gold line represents the best-fit model to the observed dust continuum.

(Dello Russo et al. 2004) over a spectral interval encompassed by that shown in Figure 3(c).

The geocentric Doppler shift of C/2018 Y1 was unusually favorable throughout our study. Most significantly, this displaced observed cometary lines of CO and CH<sub>4</sub> well away from their telluric counterpart absorptions and into regions of higher atmospheric transmittance. We detected multiple lines of CO in C/2018 Y1 (Figure 2), as reported for several previous comets observed with iSHELL (DiSanti et al. 2017; Faggi et al. 2018; Roth et al. 2018, 2020); however, owing to insufficient S/N, a robust rotational analysis (determination of  $T_{\text{rot}}$ ) as discussed above was not feasible. Instead, a  $\chi^2$  minimization was performed on the combined signal from H<sub>2</sub>O and CO contained in two M2 orders (see Table 2, footnote b). In the case of CH<sub>4</sub>, we measured a number of lines with sufficient S/N (as shown in Figure 1) to obtain robust measures of  $T_{\text{rot}}$  (Section 4.3).

A summary of our rotational analysis is presented in Table 2. Along with their respective mean  $T_{\text{rot}}$  (shown in bold), these incorporate stochastic errors and weighted variances among individual measured values. The larger spread for January 13 is consistent with C/2018 Y1 being relatively faint, resulting in lower S/N and therefore somewhat larger overall uncertainties for both individual and mean values.

Our measured  $T_{\text{rot}}$  indicates a spread among molecules. On both January 13 and February 5,  $T_{\text{rot}}$  was lower for CH<sub>3</sub>OH compared to comeasured CH<sub>4</sub> and C<sub>2</sub>H<sub>6</sub> and higher for CH<sub>4</sub> on January 13. However, given the measurement uncertainties, the extent to which these differences are meaningful is unclear. Our results appear to be in line with previous studies of comets in that, among the molecules we characterized in C/2018 Y1, a meaningful representative  $T_{\text{rot}}$  can typically be established to within an uncertainty of approximately 10 K (e.g., see Section 3.1 of Gibb et al. 2012).

### 3.2. Molecular Production Rates and Abundance Ratios for C/2018 Y1

#### 3.2.1. Nucleus-centered Production Rates

We obtained nucleus-centered production rates ( $Q_{\text{nc}}$ ) through the use of a well-established formalism (Dello Russo et al. 1998;

DiSanti et al. 2001; Villanueva et al. 2011a). Here  $Q_{\text{nc}}$  relates the observed emission line flux to the modeled fluorescence efficiency ( $g$  factor) multiplied by atmospheric transmittance at each Doppler-shifted line frequency and includes the molecular photodissociation lifetime and geometric parameters,

$$Q_{\text{nc}} = \frac{4\pi\Delta^2 F_{\text{line}}}{t_1 f(x) g_1}, \quad (1)$$

where the geocentric distance of C/2018 Y1 ( $\Delta$ ) is in meters;  $t_1$  (s) and  $g_1$  (W molecule<sup>-1</sup>) are the photodissociation lifetime and line  $g$  factor, respectively (both evaluated at  $R_h = 1$  au);  $f(x)$  is the fractional number of molecules in the coma contained within the nucleus-centered aperture (see the Appendix in Hoban et al. 1991); and  $F_{\text{line}}$  (W m<sup>-2</sup>) is the measured line flux. The ratio  $F_{\text{line}}/g_1$  pertains to signal contained within each individual spectral resolution element, whether due to a single line or a spectrally blended group of lines. For a given parent volatile, the mean column density (molecules m<sup>-2</sup>) within the nucleus-centered beam is proportional to  $Q_{\text{nc}}$  (and hence to  $F_{\text{line}}/g_1$ ) through the relation

$$N_{\text{col}} = \frac{Q_{\text{nc}}}{A_{\text{beam}}} t_1 f(x) R_h^2, \quad (2)$$

where  $R_h$  is in au. The quantity  $A_{\text{beam}} = 9.86 \times 10^{11} [\Delta(\text{au})]^2$  is the projected area (m<sup>2</sup>) of the (075 × 25) nucleus-centered beam aperture. The results of our study are presented in Table 3. For each molecule,  $Q_{\text{nc}}$  is averaged over a number of spectral resolution elements—corresponding to each isolated line or multiple blended lines—within the given echelle orders and, by extension, over multiple orders contained within each iSHELL setting. (For a general discussion relating  $Q_{\text{nc}}$  and  $N_{\text{col}}$ , see Section 3.1 in DiSanti et al. 2009.)

We assume a spherically symmetric gas outflow with speed  $v_{\text{gas}} = v_1 R_h^{-0.5}$ , where  $v_1 = 800$  m s<sup>-1</sup> is the value at  $R_h = 1$  au. The exact value of  $v_{\text{gas}}$  influences absolute production rates—these are proportional to  $v_{\text{gas}}$ —but has a negligible effect on relative abundances among parent volatiles. Additional details are found in Section 3.2.2 of DiSanti et al. (2016). Papers

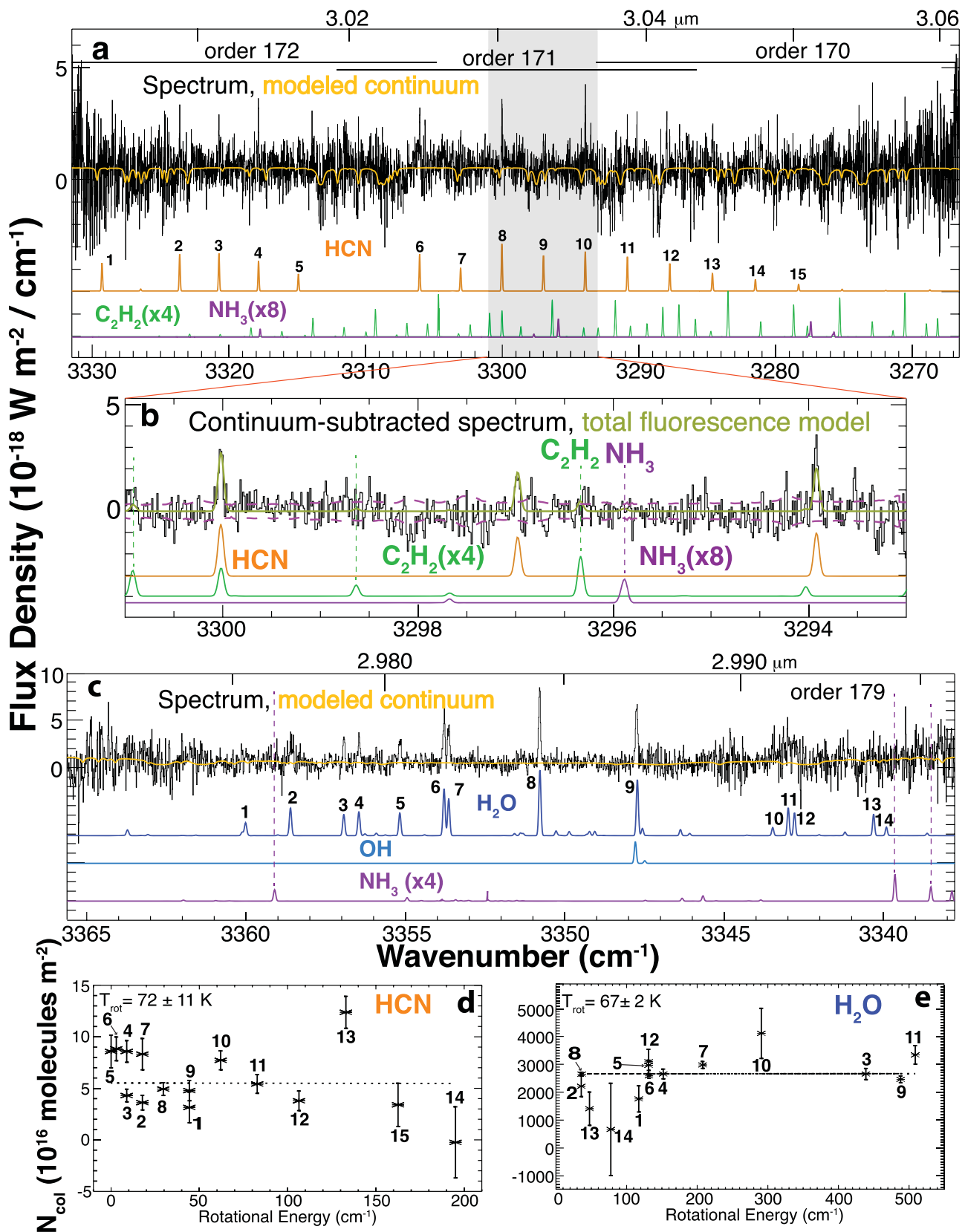


**Figure 3.** Nucleus-centered spectra of C/2018 Y1 from the Lcust setting on February 5. As in Figure 1, panel (b) shows an expanded view of emissions within order 171 (following subtraction of the dust continuum) to more clearly reveal the spectral content for  $\text{C}_2\text{H}_2$  and  $\text{NH}_3$ , for which emissions are relatively weak. Panels (d) and (e) show line-by-line rotational temperature analyses for HCN and  $\text{H}_2\text{O}$  based on the corresponding spectra in panels (a) and (c), respectively, expressed as molecular column densities (see Equations 1 and 2). Numerical labels on points correspond to lines as shown in the spectral panels.

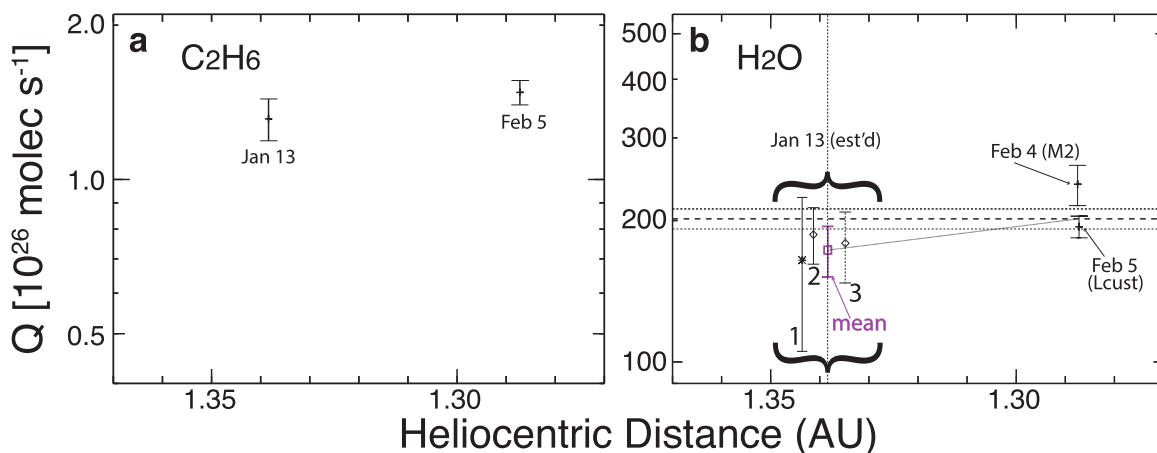


**Figure 4.** Total production rates for (a)  $C_2H_6$  and (b)  $H_2O$  in C/2018 Y1, spanning our three UT observation dates (Table 1). In panel (b), the mean  $Q(H_2O)$  (dashed horizontal line) and associated  $\pm 1\sigma$  uncertainty (dotted lines) of direct  $H_2O$  measurements on February 4 and 5 are also shown. Our estimates for  $Q(H_2O)$  on January 13 are numbered according to our three independent approaches (Section 3.2.3). For clarity, these and their mean (shown in magenta) are offset slightly in  $R_h$ .

**Table 2**

Measurements of Rotational Temperatures in C/2018 Y1a (Iwamoto)<sup>a</sup>

2019 UT Date	Molecule	$T_{rot}$ (K)	iSHELL Setting/Order(s)
Jan 13	$C_2H_6^b$	$57 \pm 4$	Lp1 orders 156–154
	$CH_3OH^b$	$45^{+6}/_{-5}$	Lp1 order 147
	$CH_4$	$79 \pm 12$	Lp1 orders 158–154
		<b><math>55 \pm 6^c</math></b>	
Feb 4	$H_2O, CO^b$	$68 \pm 4$	M2 orders 111–110
Feb 5	HCN	$72 \pm 10$	Lcust orders 172–170
	$H_2O$	$63 \pm 3$	Lcust order 179
	$C_2H_6^b$	$63 \pm 3$	Lp1 order 155
	$CH_3OH^b$	$53 \pm 5$	Lp1 order 147
	$CH_4 E_{low}, E_{up}$	$70 \pm 3, 66 \pm 2$	Lp1 orders 159–154
		<b><math>65 \pm 2^c</math></b>	

**Notes.**

<sup>a</sup>  $T_{rot}$  is reported for individual molecules, as shown for HCN and  $H_2O$  in Figures 3(d) and (e) and  $CH_4$  in Figures 8(b) and (c) based on lower and upper-state rotational energies, respectively.

<sup>b</sup>  $T_{rot}$  was measured for  $C_2H_6$  and  $CH_3OH$  through comparison among spectral intervals encompassing stronger lines. The  $H_2O$  and CO were fit simultaneously over M2 orders 111 and 110 (Figure 2) using a Levenberg–Marquardt  $\chi^2$  minimization approach (see Villanueva et al. 2008 for details).

<sup>c</sup> Bold entries denote weighted mean  $T_{rot}$  from January 13 and from February 4–5.

detailing the fluorescence models used in our analysis are as follows:  $H_2O$  (Villanueva et al. 2012b),  $C_2H_6$  (Villanueva et al. 2011b),  $CH_4$  (Gibb et al. 2003),  $CH_3OH$  (Villanueva et al. 2012a; DiSanti et al. 2013), OH (Bonev et al. 2006),  $H_2CO$  (DiSanti et al. 2006), CO (DiSanti et al. 2001; Paganini et al. 2013), HCN (Lippi et al. 2013),  $C_2H_2$  (Villanueva et al. 2011a), and  $NH_3$  (Villanueva et al. 2013).

### 3.2.2. Global Production Rates

For overall production rates, each  $Q_{nc}$  was multiplied by an appropriate growth factor (GF), determined through the well-documented “ $Q$ -curve” method of analyzing emission intensities along the slit and dating to the study of OCS in C/1995 O1 (Hale–Bopp; Dello Russo et al. 1998). Measuring signal at increasing distances from the nucleus corrects for atmospheric

seeing—which invariably suppresses signal along lines of sight passing close to the nucleus—and also mitigates the effects of a potential small drift of the comet over the course of individual ABBA spectral sequences. For all observations, we were actively guiding on C/2018 Y1; therefore, any drift was consistently within the atmospheric seeing ( $\sim 1''$ ).

The product  $Q_{nc}$  GF is taken to be the “total” (or “global”) production rate, denoted  $Q_{tot}$ . Measuring the mean of emission intensities at corresponding distances to either side of the nucleus averages over outflow asymmetries and provides the most representative measure of global production rates (see discussion in Xie & Mumma 1996). For each molecule, the mean of GFs for emissions within an instrument setting (weighted by their  $1\sigma$  uncertainties) was applied to each  $Q_{nc}$  in establishing the overall GF and thereby the corresponding  $Q_{tot}$ . Results are summarized in Table 3, and  $Q_{tot}$  for  $C_2H_6$  and  $H_2O$  (together with their  $\pm 1\sigma$  uncertainties) is shown in Figures 4(a) and (b), respectively.

The measured  $Q_{tot}$  for  $H_2O$  decreased by approximately 14% between mid-UT of the M2 and Lcust sequences on February 4 and 5, respectively (separated by approximately 21.6 hr). This, and also structure observed in our spatial profiles (see Section 4.2), may be related to rotation of the nucleus of C/2018 Y1; however, the scope of our data is insufficient to address this question. In our estimate of  $Q_{tot}(H_2O)$  on January 13, we use the mean of these two measurements (see Section 3.2.3 and Figure 4).

### 3.2.3. Estimating the Production Rate of $H_2O$ on 2019 January 13

Because  $H_2O$  emissions are not present in the 3.3–3.6  $\mu m$  region, water was not measured directly in C/2018 Y1 on January 13; therefore, direct abundance comparisons with respect to  $H_2O$  were not possible for this date. Traditionally, we use OH prompt emission lines contained in the Lp1 setting (e.g., as shown in Figure 1) as proxies for the production and spatial distribution of parent  $H_2O$  molecules in the coma (e.g., see Bonev et al. 2006 for detailed discussion).

Our study of C/2018 Y1 revealed extremely weak OH lines, weaker than expected (for a given water production rate) by a factor of nearly 2 compared with those from studies of previous comets. This apparent reduction in OH  $g$  factors seems to reflect the dramatically lower solar UV flux resulting from the

deep solar minimum that started in 2018 (Scoles 2019). For this reason, using previously established (empirical) OH  $g$  factors (Bonev et al. 2006) did not provide a reliable quantitative value for  $Q(\text{H}_2\text{O})$  on February 5. Instead, the resulting value from OH was far below  $Q(\text{H}_2\text{O})$  from the Lcust setting obtained just prior to the Lp1 observational sequence. Therefore, by extension, it is likely that OH also did not provide a faithful quantitative value for  $Q(\text{H}_2\text{O})$  on January 13. Nonetheless, to estimate  $Q(\text{H}_2\text{O})$  on this date, we were able to incorporate observed OH emissions into our analysis.

We estimated  $Q(\text{H}_2\text{O})$  on January 13 using three independent approaches.

1. We scaled  $Q(\text{H}_2\text{O})$  from February 4 to 5 by the ratio of production rates measured from OH on January 13 ( $101.8 \pm 34.2 \times 10^{26} \text{ s}^{-1}$ ) and February 5 ( $114.3 \pm 13.9 \times 10^{26} \text{ s}^{-1}$ ; Table 3):

$$Q(\text{H}_2\text{O})_{\text{January 13}} = Q(\text{H}_2\text{O})_{\text{February 4,5}} \left[ \frac{Q(\text{H}_2\text{O})_{\text{January 13, from OH}}}{Q(\text{H}_2\text{O})_{\text{February 5, from OH}}} \right]. \quad (3)$$

Here  $Q(\text{H}_2\text{O})_{\text{February 4,5}}$  denotes the mean  $Q(\text{H}_2\text{O})$  from February 4 and 5 based on direct measures of  $\text{H}_2\text{O}$  in the M2 and Lcust settings, respectively ( $198.1 \pm 11.7 \times 10^{26} \text{ s}^{-1}$ ). Assuming no change in solar UV flux (and hence in effective OH  $g$  factors) between Lp1 observations on January 13 and February 5, this results in  $Q(\text{H}_2\text{O})_{\text{January 13}} = (169 \pm 62) \times 10^{26} \text{ s}^{-1}$ , the large uncertainty being dominated by that from OH on January 13, for which the formal S/N based on the above  $Q(\text{OH})$  is only  $2.98\sigma$ . This suggests at best an overall marginal detection of OH on this date. Owing to the broader and more complex spatial distribution of  $\text{H}_2\text{O}$  apparent in our February observations, we adopted the GF measured for  $\text{CH}_3\text{OH}$  in estimating the (total) water production on January 13 (Table 3).

2. We assumed a common value for the abundance ratio  $\text{C}_2\text{H}_6/\text{H}_2\text{O}$  on January 13 ( $T_{\text{rot}} = 55 \text{ K}$ ) and February 5 ( $0.762 \pm 0.059 \times 10^{-2}$ ;  $T_{\text{rot}} = 65 \text{ K}$ ). This resulted in  $Q(\text{H}_2\text{O}) = (187 \pm 25) \times 10^{26} \text{ s}^{-1}$ .
3. We scaled our direct  $Q(\text{H}_2\text{O})_{\text{February 4,5}}$  to January 13 by assuming a heliocentric power-law dependence  $R_{\text{h}}^n$ , which is observed to be highly variable among comets. Accordingly, we assume a large range ( $n = 0$  to  $-8$ ; i.e., we assumed  $R_{\text{h}}^{-4 \pm 4}$ ). This resulted in  $Q(\text{H}_2\text{O}) = (170 \pm 28) \times 10^{26} \text{ s}^{-1}$ .

The results from these three approaches agree to well within their respective uncertainties. Accordingly, we take their mean ( $179 \pm 18 \times 10^{26} \text{ s}^{-1}$ ;  $T_{\text{rot}} = 55 \text{ K}$ ) to be our most reliable estimate of the total water production rate in C/2018 Y1 on January 13. We note that including results based on approaches 2 and 3 only results in  $179 \pm 19 \times 10^{26} \text{ s}^{-1}$ ; therefore, although including all three approaches does not change the formal value, it does improve the uncertainty somewhat, increasing the S/N of our formal  $Q(\text{H}_2\text{O})$  estimate from  $9.6\sigma$  to  $10.0\sigma$ .

Figure 4(b) illustrates these three estimates (and their mean) for  $Q(\text{H}_2\text{O})$  near 1.34 au, labeled by number and (for ease of viewing) offset slightly from one another in  $R_{\text{h}}$ . As noted, including (or excluding) point 1 does not change our estimated  $Q(\text{H}_2\text{O})$  for January 13, to three significant figures.

Our most reliable estimate is approximately 10% lower than the mean value from direct  $\text{H}_2\text{O}$  measurements in the M2 and Lcust settings on February 4 and 5, respectively ( $198 \pm 12 \times 10^{26} \text{ s}^{-1}$ ). In Section 4.1, we use this to quantify our estimate of improvements in IR sensitivity offered by iSHELL.

### 3.2.4. Abundance Ratios in C/2018 Y1

Addressing the compositional taxonomy of comets requires measuring “mixing ratios” (also termed “abundance ratios”) for a number of trace parent molecules. Simultaneous measurement of species provides the most robust means of establishing molecular abundance ratios because multiple sources of uncertainty are removed, for example, potential differential slit loss among settings and time-variable gas production and/or release. For our study of C/2018 Y1,  $\text{CH}_4$ ,  $\text{CH}_3\text{OH}$ , and  $\text{H}_2\text{CO}$  were measured simultaneously with  $\text{C}_2\text{H}_6$  on January 13 and February 5; CO was measured simultaneously with  $\text{H}_2\text{O}$  on February 4; and HCN,  $\text{C}_2\text{H}_2$ , and  $\text{NH}_3$  were measured simultaneously with  $\text{H}_2\text{O}$  on February 5. Each of these observing sequences represents a snapshot of cometary activity averaged over 1–2 hr of clock time and (on February 5) with their mid-sequence UT separated by 2.3 hr (Table 1).

Figures 5 and 6 respectively show mixing ratios as total molecular production rates divided by those of  $\text{C}_2\text{H}_6$  and  $\text{H}_2\text{O}$ . Abundance ratios relative to  $\text{H}_2\text{O}$  have traditionally been reported because water is the most abundant molecule in the vast majority of active comets. Abundance ratios  $Q(X)/Q(\text{C}_2\text{H}_6)$  are shown in Figure 5, also incorporating our estimate of  $Q(\text{H}_2\text{O})$ , shown in magenta in Figure 5(a). Similarly, values for  $Q(X)/Q(\text{H}_2\text{O})$  in Figure 6 also include those from January 13, again using our best estimate. Also shown are the mean values measured among comets, together with maxima and minima (upper and lower shaded regions, respectively). The mean abundances correspond to those in Table 4 of Dello Russo et al. (2016) and are based on 17–19 OCCs (depending on molecule). The corresponding mean values in Figure 5 are based on these same comets and determined by dividing the mean abundance ratio for each species relative to  $\text{H}_2\text{O}$  by the mean abundance ratio  $Q(\text{C}_2\text{H}_6)/Q(\text{H}_2\text{O})$  among OCCs ( $0.63\% \pm 0.10\%$ ; Dello Russo et al. 2016).

For C/2018 Y1, production rates were compared to measurements conducted closest in time of  $\text{C}_2\text{H}_6$  (in the Lp1 setting) or  $\text{H}_2\text{O}$  (as measured directly in Lcust or M2) either simultaneously or contemporaneously. In Figures 4–6, all error bars represent  $\pm 1\sigma$  uncertainties, and downward-facing arrows represent  $3\sigma$  upper limits.

In addition to the practical reason for using multiple compositional baseline molecules (as required here, given our limited C/2018 Y1 data set), such comparisons are also valuable for understanding volatile release in comets. Bonev et al. (2021) discussed taxonomic compositional baselines other than  $\text{H}_2\text{O}$ , and suggested that using both  $\text{C}_2\text{H}_6$  (a nonpolar molecule) and  $\text{H}_2\text{O}$  (a polar molecule) provides a more complete picture of cometary parent volatile composition, potentially accounting for differences in outgassing sources and how ices are associated in the nucleus.

For our study, molecules were comeasured consecutively (but separately) in the Lcust and Lp1 settings on February 5



**Table 3**  
Production Rates and Abundances in C/2018 Y1<sup>a</sup>

2019 UT Date	Setting/Order	Species	$\Gamma^b$	$Q_{nc}^c$ $10^{26}$ mol s <sup>-1</sup>	GF <sup>d</sup>	$Q_{tot}^e$ $10^{26}$ mol s <sup>-1</sup>	$X_{C_2H_6}^f$ C <sub>2</sub> H <sub>6</sub> = 1.0	$X_{H_2O}^g$ H <sub>2</sub> O = 100
<b>Jan 13</b>	Lp1/158	CH <sub>4</sub>	9.181	0.803 ± 0.098	<i>1.512 ± 0.197</i>	1.22 ± 0.19		
		OH*		37.7 ± 30.2		71.6 ± 58.1		
	Lp1/157	CH <sub>4</sub>	9.096	0.679 ± 0.068	<i>1.511 ± 0.294</i>	1.03 ± 0.14		
		OH*		152.2 ± 140.4		230.4 ± 213.7		
	Lp1/156	CH <sub>4</sub>	8.904	1.12 ± 0.22	<i>1.521 ± 0.329</i>	1.70 ± 0.38		
	Lp1/155	C <sub>2</sub> H <sub>6</sub>	8.413	0.932 ± 0.059	<i>1.407 ± 0.155</i>	1.31 ± 0.13		
		CH <sub>4</sub>		0.378 ± 0.185		0.573 ± 0.285		
		CH <sub>3</sub> OH		5.00 ± 0.38	<i>1.863 ± 0.269</i>	9.52 ± 1.46		
	Lp1/154	OH*		17.6 ± 24.6		33.4 ± 47.0		
		C <sub>2</sub> H <sub>6</sub>	8.341	0.935 ± 0.070	<i>1.407 ± 0.135</i>	1.32 ± 0.14		
		CH <sub>3</sub> OH		3.76 ± 0.52		7.16 ± 1.38		
	Lp1/147	CH <sub>3</sub> OH	7.992	5.65 ± 0.39	<i>2.243 ± 0.770</i>	10.76 ± 1.62		
		H <sub>2</sub> CO		<0.474		<0.902		
		OH*		93.5 ± 39.0		178 ± 78		
	Lp1/144	H <sub>2</sub> CO	7.557	<0.350		<0.666		
		OH*		203 ± 59		386 ± 122		
		C <sub>2</sub> H <sub>6</sub>		0.933 ± 0.053	<b>1.41 ± 0.10</b>	1.31 ± 0.12	<b>1.0</b>	<b>0.73 ± 0.11</b>
		CH <sub>4</sub>		0.713 ± 0.058	<b>1.51 ± 0.15</b>	1.08 ± 0.14	<b>0.82 ± 0.12</b>	<b>0.60 ± 0.11</b>
		CH <sub>3</sub> OH		5.12 ± 1.16	<b>1.904 ± 0.254</b>	9.75 ± 1.43	<b>7.4 ± 1.2</b>	<b>5.5 ± 1.0</b>
	H <sub>2</sub> CO		<0.281	<b>(1.904)</b>	<0.536	<b>&lt;0.41</b>	<b>&lt;0.30</b>	
	OH*		53.5 ± 16.5	<b>(1.904 ± 0.254)</b>	101.8 ± 34.2			
	H <sub>2</sub> O <sup>g</sup>		“best estimate” (Section 3.2.3)		<i>179 ± 18</i>	<b>129 ± 18</b>	<b>100</b>	
	cont			<b>1.34 ± 0.11</b>				
<b>Feb 4</b>	M2/111	H <sub>2</sub> O	6.84	114.8 ± 8.7	<i>2.318 ± 0.205</i>	269.1 ± 28.3		
		CO		1.44 ± 0.18	<i>1.766 ± 0.265</i>	2.05 ± 0.35		
	M2/110	H <sub>2</sub> O	6.58	89.71 ± 9.07	<i>2.767 ± 0.408</i>	210.3 ± 26.2		
		CO		1.48 ± 0.12	<i>1.342 ± 0.130</i>	2.11 ± 0.31		
	M2/103	H <sub>2</sub> O		89.13 ± 11.88	<i>1.894 ± 0.486</i>	209.0 ± 31.8		
		H <sub>2</sub> O		102.0 ± 6.8 <sup>c</sup>	<b>2.344 ± 0.172</b>	239.0 ± 23.7	<b>162 ± 18</b>	<b>100</b>
		CO		1.47 ± 0.11	<b>1.425 ± 0.168</b>	2.087 ± 0.242	<b>1.41 ± 0.18</b>	<b>0.87 ± 0.13</b>
	cont			<b>1.23 ± 0.04</b>				
<b>Feb 5</b>	Lcust/182	H <sub>2</sub> O	14.82	103.7 ± 5.2	<i>1.919 ± 0.041</i>	194.8 ± 10.4		
		NH <sub>3</sub>		<17.9		<35.2		
	Lcust/179	H <sub>2</sub> O	15.22	99.5 ± 5.2	<i>1.803 ± 0.062</i>	186.8 ± 10.2		
		NH <sub>3</sub>		<1.95		<3.82		
	Lcust/175	H <sub>2</sub> O	14.99	108.4 ± 6.0	<i>1.812 ± 0.114</i>	203.5 ± 11.9		
		NH <sub>3</sub>		<0.487		<0.955		
	Lcust/172	HCN	14.79	0.191 ± 0.015	<i>2.017 ± 0.378</i>	0.392 ± 0.046		
		C <sub>2</sub> H <sub>2</sub>		0.143 ± 0.042	<i>1.715 ± 0.281</i>	0.257 ± 0.080		
		NH <sub>3</sub>		<1.43		<2.80		
	Lcust/171	H <sub>2</sub> O		69.64 ± 14.63		130.8 ± 27.6		
		HCN	15.17	0.202 ± 0.015	<i>2.056 ± 0.202</i>	0.413 ± 0.047		
		C <sub>2</sub> H <sub>2</sub>		0.078 ± 0.016	<i>2.259 ± 0.372</i>	0.140 ± 0.032		
	Lcust/170	NH <sub>3</sub>		<0.484		<0.950		
		HCN	15.11	0.186 ± 0.027		0.381 ± 0.064		
		C <sub>2</sub> H <sub>2</sub>		0.091 ± 0.016	1.409 ± 0.134	0.164 ± 0.034		
		NH <sub>3</sub>		<0.551		<1.08		
		H <sub>2</sub> O		103.3 ± 5.4	<b>1.878 ± 0.033</b>	194.1 ± 10.3	<b>131 ± 10</b>	<b>100</b>
HCN			0.196 ± 0.008	<b>2.047 ± 0.178</b>	0.401 ± 0.043	<b>0.27 ± 0.03</b>	<b>0.21 ± 0.02</b>	
C <sub>2</sub> H <sub>2</sub>			0.088 ± 0.011	<b>(1.8 ± 0.2)</b>	0.159 ± 0.027	<b>0.11 ± 0.02</b>	<b>0.082 ± 0.013</b>	
NH <sub>3</sub>		<0.282	<b>(1.96)</b>	<0.554	<b>&lt;0.37</b>	<b>&lt;0.29</b>		
	cont			<b>1.54 ± 0.05</b>				
<b>Feb 5</b>	Lp1/159	CH <sub>4</sub>	9.182	0.616 ± 0.051	<i>1.530 ± 0.178</i>	0.909 ± 0.082		
	Lp1/158	CH <sub>4</sub>	8.284	0.699 ± 0.047	<i>1.442 ± 0.127</i>	1.031 ± 0.079		
		OH*		68.51 ± 8.76	<i>1.828 ± 0.277</i>	117.8 ± 18.2		
	Lp1/157	CH <sub>4</sub>	8.202	0.720 ± 0.042	<i>1.472 ± 0.065</i>	1.063 ± 0.072		
		OH*		83.0 ± 27.2	<i>1.691 ± 0.176</i>	142.8 ± 48.4		
	Lp1/156	CH <sub>4</sub>	7.967	0.798 ± 0.076	<i>1.533 ± 0.228</i>	1.177 ± 0.120		
	Lp1/155	C <sub>2</sub> H <sub>6</sub>		1.091 ± 0.055	<i>1.427 ± 0.046</i>	1.535 ± 0.085		
		CH <sub>4</sub>		0.895 ± 0.070		1.321 ± 0.114		

**Table 3**  
(Continued)

2019 UT Date	Setting/Order	Species	$\Gamma^b$	$Q_{nc}^c$ $10^{26} \text{ mol s}^{-1}$	GF <sup>d</sup>	$Q_{tot}^e$ $10^{26} \text{ mol s}^{-1}$	$X_{C_2H_6}^f$ C <sub>2</sub> H <sub>6</sub> = 1.0	$X_{H_2O}^g$ H <sub>2</sub> O = 100
		CH <sub>3</sub> OH		3.687 ± 0.203	<i>1.619 ± 0.169</i>	5.651 ± 0.422		
	Lp1/154	OH*		60.26 ± 7.79		103.7 ± 16.2		
		C <sub>2</sub> H <sub>6</sub>		0.967 ± 0.050	<i>1.391 ± 0.040</i>	1.360 ± 0.077		
		CH <sub>4</sub>		0.590 ± 0.149		0.870 ± 0.221		
	Lp1/147	CH <sub>3</sub> OH	7.434	3.92 ± 0.23	<i>1.537 ± 0.201</i>	6.00 ± 0.47		
		CH <sub>3</sub> OH		4.14 ± 0.22	<i>1.503 ± 0.097</i>	6.34 ± 0.47		
		H <sub>2</sub> CO		<0.134		<0.231		
	Lp1/144	OH*	7.064	76.08 ± 11.96		130.9 ± 23.5		
		H <sub>2</sub> CO		<0.0947		<0.163		
		OH*		64.22 ± 16.01	<i>1.454 ± 0.743</i>	110.5 ± 29.2		
		C <sub>2</sub> H <sub>6</sub>		1.052 ± 0.053	<b>1.406 ± 0.030</b>	1.479 ± 0.081	<b>1.0</b>	<b>0.76 ± 0.06</b>
		CH <sub>4</sub>		0.7171 ± 0.0388	<b>1.475 ± 0.053</b>	1.058 ± 0.069	<b>0.72 ± 0.03</b>	<b>0.55 ± 0.05</b>
		CH <sub>3</sub> OH		3.918 ± 0.203	<b>1.533 ± 0.077</b>	6.005 ± 0.435	<b>4.1 ± 0.2</b>	<b>3.1 ± 0.3</b>
		H <sub>2</sub> CO		<0.0776	<b>(1.7)</b>	<0.133	<b>&lt;0.090</b>	<b>&lt;0.069</b>
fr o158,157,155,147,144:		OH*		66.46 ± 5.65	<b>(1.72 ± 0.15)</b>	114.3 ± 13.9		
		cont			<b>1.27 ± 0.08</b>			

**Notes.**

<sup>a</sup> Values assume rotational temperatures of 55 K on January 13 and 65 K on February 4 and 5 based on the mean value from excitation analyses of CH<sub>4</sub>, C<sub>2</sub>H<sub>6</sub>, and CH<sub>3</sub>OH on January 13 and of these molecules plus H<sub>2</sub>O and HCN on February 5, as shown in Table 2. All uncertainties represent 1 $\sigma$ , and upper limits (for NH<sub>3</sub> and H<sub>2</sub>CO) represent 3 $\sigma$ .

<sup>b</sup> Calibration factor [ $10^{-18} \text{ W m}^{-2} (\text{cm}^{-1})^{-1} / (\text{ADU s}^{-1})$ ], from observations of the IR flux standards listed in Table 1. An uncertainty of  $\pm 5\%$  in absolute calibration is included in all production rates and propagated through to total production rates, as discussed in Section 3.2.2.

<sup>c</sup> Production rate based on a nucleus-centered aperture having an angular extent  $0''.75 \times 2''.5$ . The weighted mean  $Q_{nc}$  for species within each iSHELL setting is shown in bold.

<sup>d</sup> Slit loss factor (GF) used to convert  $Q_{nc}$  to total (i.e., global) production rate ( $Q_{tot}$ ; Section 3.2.2). The GF was measured for one or more simultaneously observed emission lines having high S/N. Italicized values are those measured for emissions within specific echelle orders. Mean GF values (shown in bold with corresponding molecules) are applied to the mean  $Q_{nc}$  within each iSHELL setting. Values assumed for species having insufficient S/N (OH\*, H<sub>2</sub>CO, NH<sub>3</sub>) are shown in parentheses. For H<sub>2</sub>CO and OH\* on January 13, the GF measured for CH<sub>3</sub>OH is adopted. On February 5, the mean GFs for OH\* and C<sub>2</sub>H<sub>6</sub> are  $1.719 \pm 0.146$  and  $1.794 \pm 0.183$ ; hence, respective values of  $1.72 \pm 0.15$  and  $1.8 \pm 0.2$  are assumed for these two species.

<sup>e</sup> Total production rate. All uncertainties in  $Q_{tot}$  incorporate those in both GF and  $Q_{nc}$ , and (as for  $Q_{nc}$ ) also an assumed uncertainty of  $\pm 5\%$  in  $\Gamma$ . The value for H<sub>2</sub>O on January 13 ( $179 \pm 18$ ) represents our “best estimate” from Section 3.2.3, and is therefore shown in italics.

<sup>f</sup> Molecular abundance relative to C<sub>2</sub>H<sub>6</sub> = 1.0. All February entries use the total  $Q(C_2H_6)$  from February 5.

<sup>g</sup> Molecular abundance relative to H<sub>2</sub>O in % (i.e., relative to H<sub>2</sub>O = 100). January 13  $X_{H_2O}$  entries (in bold italics) use our “best estimate” for  $Q(H_2O)$  ( $179 \pm 18 \times 10^{26} \text{ molecules s}^{-1}$ ; Section 3.2.3). February entries are based on direct measures of  $Q(H_2O)$  on each date, either simultaneous (CO on February 4; HCN, C<sub>2</sub>H<sub>6</sub>, and NH<sub>3</sub> on February 5) or contemporaneous (C<sub>2</sub>H<sub>6</sub>, CH<sub>4</sub>, and CH<sub>3</sub>OH on February 5).

over a period encompassing approximately 3 hr (Table 1). With two exceptions, minima and maxima in Figure 6 refer to OCCs, and individual comets are identified and references cited in Table 3 of DiSanti et al. (2018). In the case of CO, the range of minimum values shown (0.15%–0.45%) is taken from Hubble Space Telescope observations of JFC 103P/Hartley 2 (Weaver et al. 2011). For CH<sub>3</sub>OH/H<sub>2</sub>O, the maximum value corresponds to JFC 252P/LINEAR ( $4.87\% \pm 0.34\%$ ; Paganini et al. 2019), representing the largest methanol abundance measured among comets prior to our value for January 13 (Table 3). Recently reported extrema are for ecliptic comet 2P/Encke, postperihelion during its 2017 apparition (C<sub>2</sub>H<sub>6</sub>/H<sub>2</sub>O =  $0.037\% \pm 0.005\%$  and C<sub>2</sub>H<sub>2</sub>/H<sub>2</sub>O < 0.007%; Roth et al. 2018). These last two abundance ratios (for C<sub>2</sub>H<sub>6</sub> and C<sub>2</sub>H<sub>2</sub>) represent minima among all comets measured to date.

The abundance ratios shown in Figures 5 and 6 were established at the most probable rotational temperature on each date ( $T_{rot} = 55 \text{ K}$  on January 13 and  $65 \text{ K}$  on February 4 and 5). Assuming a similar  $T_{rot}$  is valid among parent molecules (as is typical; Gibb et al. 2012), its precise value has relatively little affect on abundance ratios (see Table 4 and discussion in Section 4.4).

**4. Discussion**

Our high-resolution IR study of C/2018 Y1 has advanced the field of parent volatile composition in comets in significant ways. We identify three principal results that warrant discussion. (1) Sensitivity limits have been extended (Section 4.1), including the ability to obtain useful spatial information along lines of sight displaced from the nucleus and permitting a comparison of emission intensities (spatial profiles) for gas and dust (Section 4.2). (2) The continuous-wavelength coverage of iSHELL coupled with the highly favorable geocentric Doppler shift of C/2018 Y1 during our observations allowed for a mostly complete sampling of CH<sub>4</sub> (Section 4.3). (3) As is commonly found from our ongoing compositional taxonomy of comets, our measurements of C/2018 Y1 have implications for the processing history of constituent ices prior to their being incorporated into the nucleus (Section 4.4). Additional context is provided through comparisons with previous compositional studies of ices housed in comet nuclei (i.e., native ices).

**4.1. Recent Advancements in Sensitivity Afforded by iSHELL**

The relative brightness of spectral lines can be estimated using an infrared figure of merit (FoM), expressed as

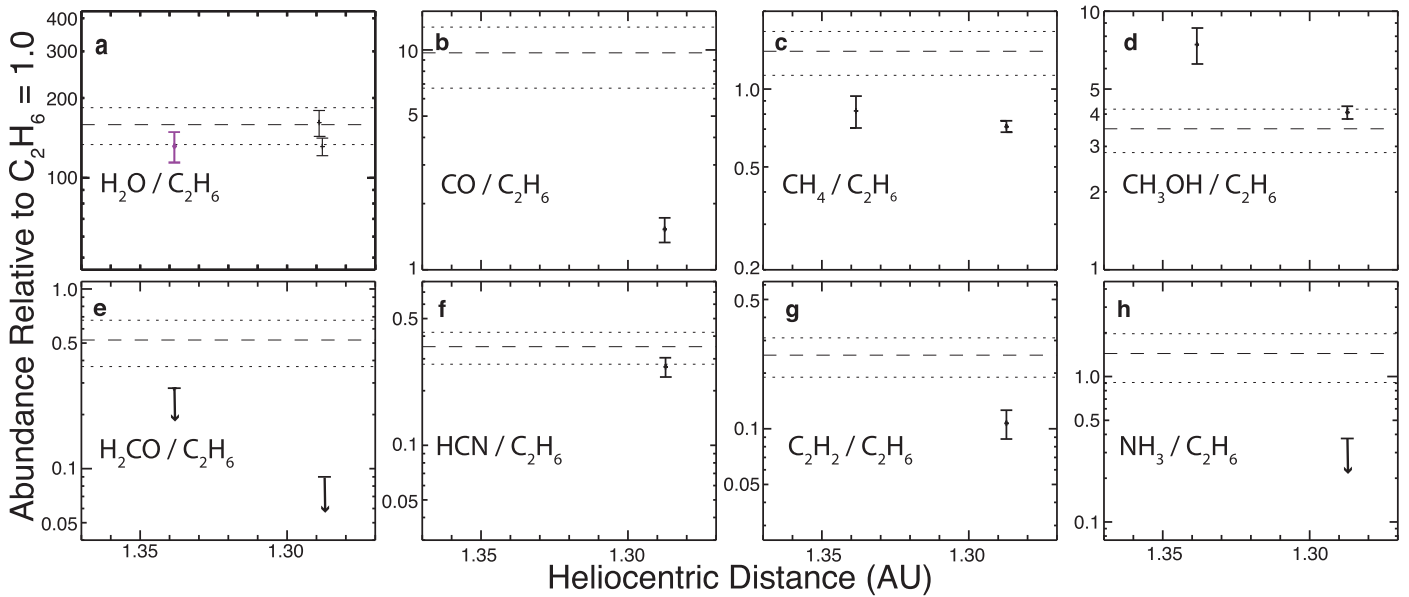


**Figure 5.** Mixing ratios relative to simultaneously or contemporaneously measured  $C_2H_6$  in C/2018 Y1, together with mean values (dashed line) and  $\pm 1\sigma$  uncertainties (dotted lines) reported among OCCs.

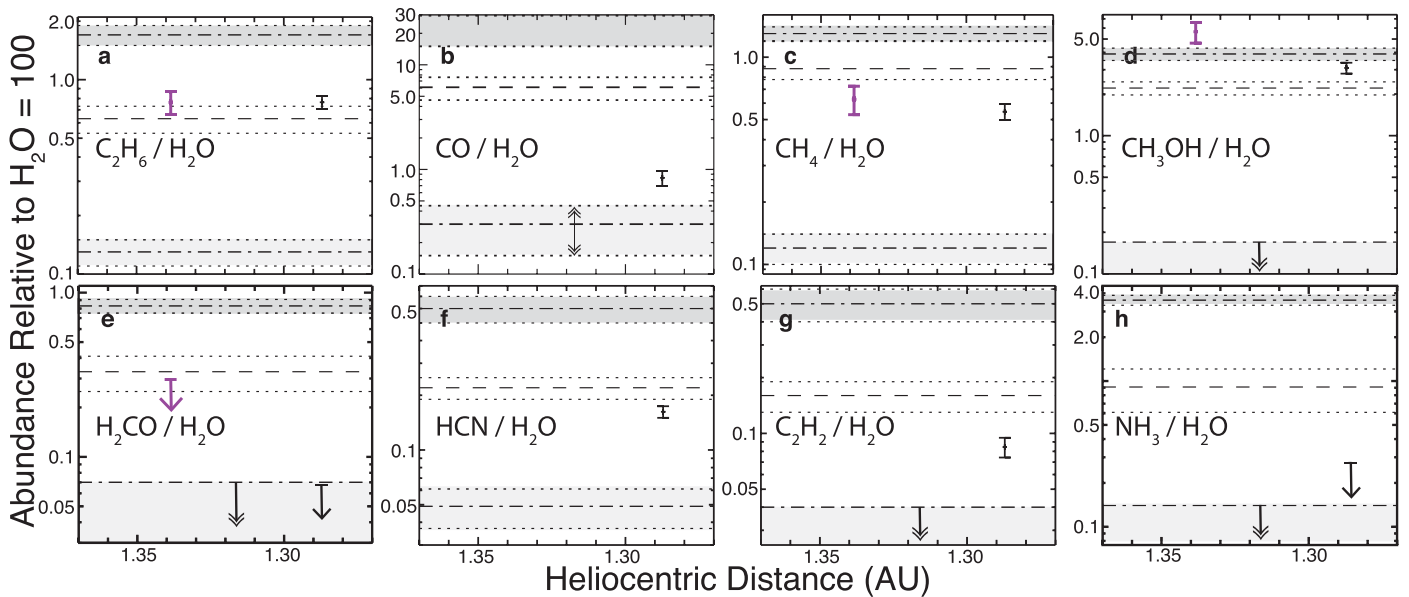


**Figure 6.** Similar to Figure 5 but showing mixing ratios (in percent) relative to  $H_2O$ . In addition to mean values, the minimum (lower shaded regions; double-headed arrows indicate  $3\sigma$  upper limits) and maximum (upper shaded regions) are shown together with their respective  $\pm 1\sigma$  uncertainties.

$FoM = 10^{-29} Q(R_h) R_h^{-1.5} \Delta^{-1}$  (e.g., see Table 1 in Mumma et al. 2003), with  $Q(R_h)$  representing the  $H_2O$  production rate measured at heliocentric distance  $R_h$  and with  $R_h$  and  $\Delta$  expressed in au. In a practical sense, for a given IR spectrograph, the FoM is used to assess the amount of time required to achieve adequate S/N, especially for species having weaker emission lines (e.g.,  $C_2H_2$  in the Lcust setting).

Prior to iSHELL becoming available for use in late 2016, high-resolution spectroscopy at the IRTF required using the legacy facility near-IR spectrograph, CSHELL (Tokunaga et al. 1990), which became available for use by the community in 1992 and was the only such instrument for nearly a decade. With CSHELL, obtaining unambiguous spatial information with sufficient S/N (particularly along lines displaced from the

nucleus) required an FoM of  $\sim 0.5$ – $0.7$  or higher for nighttime observations and 1 or higher for daytime observations.

Our study of C/2018 Y1 has extended sensitivity limits to substantially lower values. Direct measurements of  $H_2O$  on February 4 and 5 imply  $FoM = 0.31$ – $0.33$ ; however, the cometary emissions we observed on January 13 were much weaker (by a factor of  $\sim 3$ ; compare Figures 1(a) and (b)). Our best estimate  $Q(H_2O) = 179 \pm 18 \times 10^{26} \text{ s}^{-1}$  on January 13 (see Section 3.2.3) translates to  $FoM = 0.10 \pm 0.01$ . Despite this low FoM, we nonetheless obtained reliable spatial profiles and GFs for three parent molecules ( $CH_4$ ,  $C_2H_6$ , and  $CH_3OH$ ) on January 13 (see Table 3 and Figure 7(a)), even given the relatively modest on-source integration time (approximately 1 hr).

**Table 4**  
Molecular Abundances Relative to C<sub>2</sub>H<sub>6</sub> and H<sub>2</sub>O in C/2018 Y1 (Iwamoto)

<b>Jan 13</b>											
Lp1	Abundance Relative to $Q(\text{C}_2\text{H}_6) = 1.0$					Abundance Relative to $Q(\text{H}_2\text{O}) = 100$					
$T_{\text{rot}} =$	40	50	55	60	70	50	55	60	70		
$Q(\text{C}_2\text{H}_6)[\text{E}26 \text{ s}^{-1}]$ :	$1.193 \pm 0.112$	$1.275 \pm 0.119$	$1.313 \pm 0.123$	$1.347 \pm 0.126$	$1.409 \pm 0.131$	$Q(\text{H}_2\text{O})[\text{E}26 \text{ s}^{-1}]^{\text{a}}$	$175 \pm 18$	$179 \pm 18$	$178 \pm 19$	$179 \pm 19$	
Molecule											
C <sub>2</sub> H <sub>6</sub>	1.0	1.0	1.0	1.0	1.0		$0.73 \pm 0.11$	$0.73 \pm 0.11$	$0.77 \pm 0.11$	$0.79 \pm 0.12$	
CH <sub>4</sub>	$0.61 \pm 0.09$	$0.76 \pm 0.11$	$0.82 \pm 0.12$	$0.88 \pm 0.12$	$1.00 \pm 0.14$		$0.55 \pm 0.09$	$0.60 \pm 0.11$	$0.68 \pm 0.11$	$0.78 \pm 0.14$	
CH <sub>3</sub> OH	$6.8 \pm 1.1$	$7.3 \pm 1.2$	$7.4 \pm 1.2$	$7.6 \pm 1.2$	$7.8 \pm 1.2$		$5.3 \pm 1.0$	$5.5 \pm 1.0$	$6.1 \pm 1.2$	$6.1 \pm 1.2$	
H <sub>2</sub> CO	<0.41	<0.40	<0.41	<0.42	<0.44		<0.29	<0.30	<0.32	<0.35	
OH <sup>*</sup>	$85.0 \pm 30.1$	$79.9 \pm 28.1$	$77.6 \pm 27.3$	$72.9 \pm 26.4$	$65.0 \pm 24.8$		$58.3 \pm 21.2$	$56.9 \pm 21.1$	$57.9 \pm 21.0$	$53.8 \pm 20.6$	
OH <sup>*</sup> -corr <sup>d</sup>	<i><math>142 \pm 20</math></i>	<i><math>132 \pm 19</math></i>	<i><math>129 \pm 18</math></i>	<i><math>126 \pm 18</math></i>	<i><math>121 \pm 17</math></i>						
<b>Feb 4</b>											
M2	Abundance relative to $Q(\text{C}_2\text{H}_6)$ (from Feb 5) = 1.0					Abundance relative to $Q(\text{H}_2\text{O}) = 100$					
$T_{\text{rot}} =$	50	60	65	70	80	50	60	65	70	80	
$Q(\text{H}_2\text{O}) [\text{E}26 \text{ s}^{-1}]$ :	$215.1 \pm 21.4$	$231.2 \pm 23.0$	$239.0 \pm 23.7$	$246.5 \pm 24.5$	$260.4 \pm 25.8$						
H <sub>2</sub> O	$158 \pm 18$	$160 \pm 18$	$162 \pm 18$	$163 \pm 18$	$165 \pm 19$	100	100	100	100	100	
CO	$1.36 \pm 0.17$	$1.39 \pm 0.18$	$1.41 \pm 0.18$	$1.43 \pm 0.18$	$1.48 \pm 0.19$	$0.86 \pm 0.13$	$0.87 \pm 0.13$	$0.87 \pm 0.13$	$0.88 \pm 0.13$	$0.90 \pm 0.14$	
<b>Feb 5</b>											
Lp1	Abundance relative to $Q(\text{C}_2\text{H}_6) = 1.0$					Abundance relative to $Q(\text{H}_2\text{O}) = 100$					
$T_{\text{rot}} =$	50	60	65	70	80	50	60	65	70	80	
$Q(\text{C}_2\text{H}_6)[\text{E}26 \text{ s}^{-1}]$ :	$1.358 \pm 0.075$	$1.441 \pm 0.079$	$1.479 \pm 0.081$	$1.514 \pm 0.083$	$1.580 \pm 0.087$						
C <sub>2</sub> H <sub>6</sub>	1.0	1.0	1.0	1.0	1.0	$0.71 \pm 0.05$	$0.75 \pm 0.06$	$0.76 \pm 0.06$	$0.78 \pm 0.06$	$0.81 \pm 0.06$	
CH <sub>4</sub>	$0.60 \pm 0.03$	$0.68 \pm 0.32$	$0.72 \pm 0.03$	$0.75 \pm 0.04$	$0.80 \pm 0.04$	$0.42 \pm 0.04$	$0.51 \pm 0.04$	$0.55 \pm 0.05$	$0.58 \pm 0.05$	$0.65 \pm 0.05$	
CH <sub>3</sub> OH	$3.8 \pm 0.2$	$4.0 \pm 0.2$	$4.1 \pm 0.2$	$4.0 \pm 0.2$	$4.2 \pm 0.2$	$2.7 \pm 0.2$	$3.0 \pm 0.3$	$3.1 \pm 0.3$	$3.1 \pm 0.3$	$3.4 \pm 0.3$	
H <sub>2</sub> CO	<0.084	<0.088	<0.090	<0.084	<0.096	<0.059	<0.066	<0.069	<0.065	<0.078	
OH <sup>*</sup>	$89.6 \pm 9.9$	$80.9 \pm 9.1$	$77.3 \pm 8.8$	$74.0 \pm 8.4$	$68.6 \pm 7.9$	$63.2 \pm 8.3$	$60.4 \pm 8.0$	$58.9 \pm 7.9$	$57.7 \pm 7.7$	$55.4 \pm 7.5$	
OH <sup>*</sup> -corr <sup>d</sup>	<i><math>143 \pm 16</math></i>	<i><math>135 \pm 15</math></i>	<i><math>131 \pm 15</math></i>	<i><math>128 \pm 15</math></i>	<i><math>123 \pm 14</math></i>	<i><math>101 \pm 13</math></i>	<i><math>101 \pm 13</math></i>	<i><math>100 \pm 13</math></i>	<i><math>100 \pm 13</math></i>	<i><math>99 \pm 13</math></i>	
Lcust						$Q(\text{H}_2\text{O})[\text{E}26 \text{ s}^{-1}]$ :	$192.4 \pm 10.2$	$192.9 \pm 10.3$	$194.1 \pm 10.3$	$194.3 \pm 10.3$	$195.5 \pm 10.4$
H <sub>2</sub> O	$142 \pm 11$	$134 \pm 10$	$131 \pm 10$	$128 \pm 10$	$124 \pm 10$	100	100	100	100	100	
HCN	$0.27 \pm 0.03$	$0.27 \pm 0.03$	$0.27 \pm 0.03$	$0.27 \pm 0.03$	$0.27 \pm 0.03$	$0.19 \pm 0.02$	$0.20 \pm 0.02$	$0.21 \pm 0.02$	$0.21 \pm 0.02$	$0.22 \pm 0.02$	
C <sub>2</sub> H <sub>2</sub>	$0.10 \pm 0.02$	$0.11 \pm 0.02$	$0.11 \pm 0.02$	$0.11 \pm 0.02$	$0.11 \pm 0.02$	$0.071 \pm 0.012$	$0.079 \pm 0.013$	$0.082 \pm 0.013$	$0.085 \pm 0.014$	$0.091 \pm 0.014$	
NH <sub>3</sub>	<0.33	<0.35	<0.37	<0.38	<0.40	<0.23	<0.26	<0.29	<0.29	<0.33	

**Notes.**

<sup>a</sup> The values of  $Q(\text{H}_2\text{O})$  for January 13 represent “best estimates” based on approaches 1–3 as discussed in Section 3.2.3, as are abundance ratios relative to H<sub>2</sub>O for trace molecules in the Lp1 setting.

<sup>b</sup> Entries “OH-corr<sup>d</sup>” are abundance ratios using best-estimate values from approaches 1–3 (Section 3.2.3) relative to C<sub>2</sub>H<sub>6</sub> on January 13 and C<sub>2</sub>H<sub>6</sub> and H<sub>2</sub>O on February 5. Accordingly, these entries are in italics, as are January 13 values for  $Q(\text{H}_2\text{O})$  and abundance ratios relative to H<sub>2</sub>O. Entries relative to H<sub>2</sub>O on January 13 are not shown, since by definition, these = 100.0 for all  $T_{\text{rot}}$ .



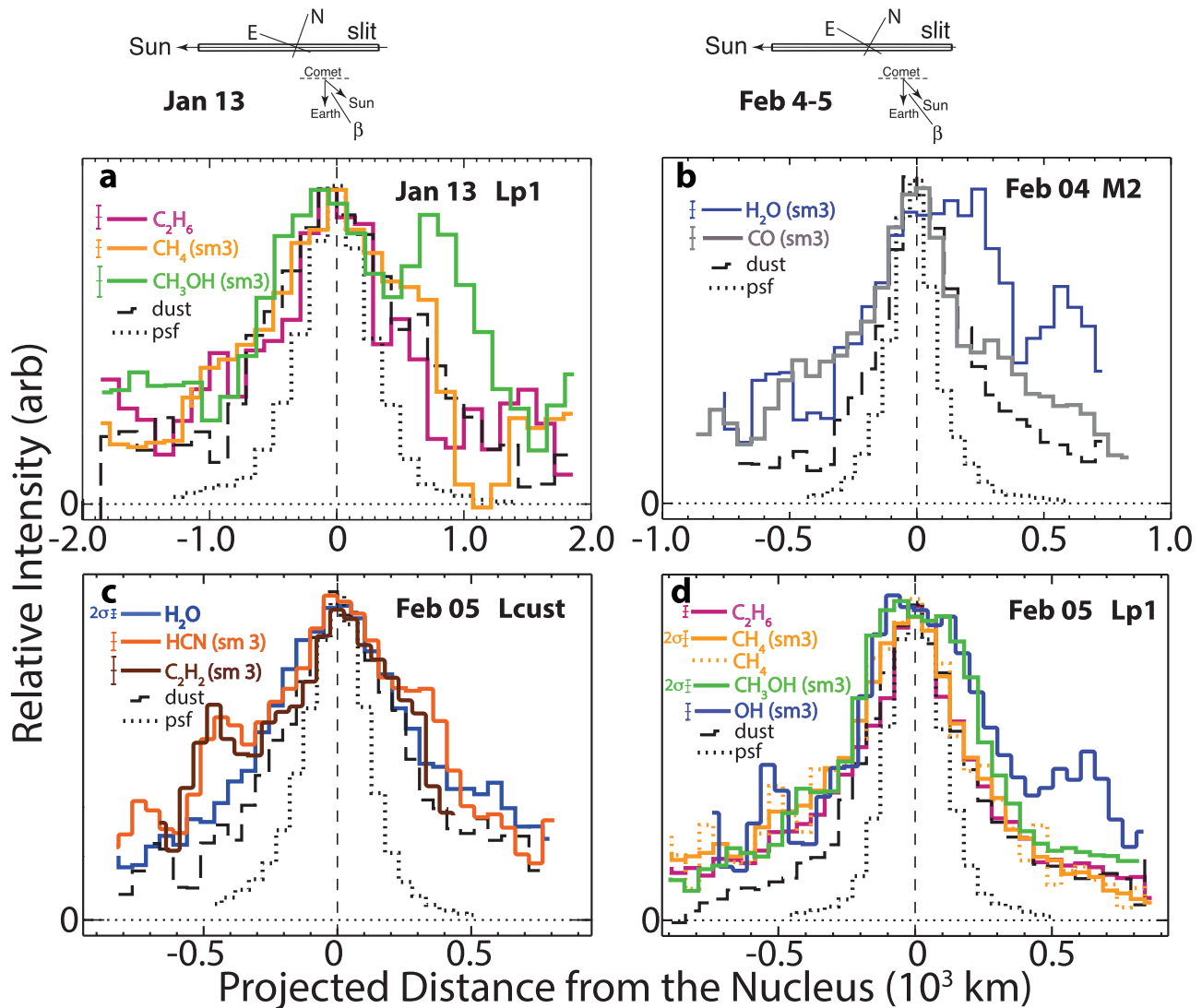


**Figure 7.** Spatial profiles of emissions in C/2018 Y1. On all dates, the slit was oriented along the Sun–comet direction, with the Sun to the left as indicated. Also depicted is the solar phase angle (denoted  $\beta$ ), which decreased from  $46^\circ$  to  $36^\circ$  over the time encompassed by our study.

#### 4.2. Comparisons among Spatial Profiles of Emissions

The powerful iSHELL spectrograph allowed for comeasuring the spatial distributions of emissions from volatiles and dust in the coma of C/2018 Y1 along projected solar and antisolar directions on three dates. The profiles of the emissions so recorded illustrate the synergy between IR temporal and spatial studies. Changes in observed spatial profiles indicate temporal variations in outgassing patterns, potentially as the root cause for time-variable coma abundances (see Section 4.4.2). The ultimate goal of assessing such temporal variations is to tie them to potential differences in composition among housed ices representing distinct active regions of the nucleus.

Figure 7 shows spatial profiles of gas and dust (continuum) emission along the slit. The profiles in each panel are measured simultaneously, thereby allowing direct comparison of the outflow of gas and dust into sunward- and antisunward-facing hemispheres as projected onto the sky plane and averaged over the times covered by each observation sequence (each iSHELL setting in Table 1). It is important to note that profiles for all species in each panel represent their simultaneously observed distributions, spatially registered to coaligned continuum

profiles from each contributing order. These are used to establish GFs for individual volatiles (and dust) and thereby to determine overall gas production rates as discussed in Section 3.2.2.

In general, profiles for the polar-bonded molecules  $\text{H}_2\text{O}$  and  $\text{CH}_3\text{OH}$  in C/2018 Y1 showed more complex structure than those of either the dust continuum or nonpolar ( $\text{CH}_4$ ,  $\text{C}_2\text{H}_6$ ) or weakly polar (CO) molecules, particularly in the projected antisunward-facing hemisphere. This may indicate regions of the coma containing more polar-rich icy grains. We next address each panel in Figure 7, noting that use of the terms “sunward” and “antisunward” refers to projection onto the sky plane into sunward- and antisunward-facing hemispheres, respectively. Rather than attempting to explain the fine structure aspects of our observed spatial profiles (e.g., lower-intensity side peaks), we instead concentrate more on their general shapes, such as relative widths and sunward- versus antisunward-facing asymmetries or lack thereof.

To improve S/N, several profiles in Figure 7 were smoothed using a sliding three-row (of spatial extent  $\sim 05$ ) unweighted average; this is indicated by “(sm3)” in the panel legends. Additionally, in order to better assess the profile shape and

structure, we also show  $\pm 1\sigma$  stochastic uncertainty levels ( $\pm 2\sigma$  levels where indicated) in the panel legends.

With the largest geocentric distance of all observations included in our study ( $\Delta = 1.178$  au), January 13 (Figure 7(a)) afforded the most extensive spatial coverage, to projected distances ( $\rho$ ) approaching  $2 \times 10^3$  km on either side of the nucleus. On this date, CH<sub>3</sub>OH was much broader than C<sub>2</sub>H<sub>6</sub> or CH<sub>4</sub> and most notably exhibited considerable antisunward intensity enhancement that peaked around  $\rho = 700$ –800 km from the nucleus.

A natural question is whether H<sub>2</sub>O showed similar enhancement, as might be expected if both this and CH<sub>3</sub>OH were housed in polar ice-dominated grains. However, because H<sub>2</sub>O was not measured directly on January 13, and we were unable to obtain a reliable spatial profile for comeasured OH prompt emission lines owing to their weaker-than-expected intensities (Section 3.2.3), we were unable to test this possibility from those observations.

On February 4, both H<sub>2</sub>O and CO showed similar sunward-facing intensities that were broader than the comeasured dust continuum profile. The H<sub>2</sub>O was greatly enhanced antisunward, with a broad central distribution and a secondary peak near 600 km. The CO was steeper antisunward to  $\rho \sim 200$  km, beyond which it displayed a relatively broad “skirt” that remained well above the comeasured dust continuum. As with January 13, this could indicate a distinct release from ices of differing polar fractions, which in turn may reflect inhomogeneous distributions in the nucleus.

On February 5, all profiles measured in the Lcust setting were relatively broad. This includes HCN, which, although a polar molecule, has revealed a spatial distribution more closely associated with nonpolar molecules (e.g., C<sub>2</sub>H<sub>6</sub>) in some comets, most notably C/2007 W1 Boattini (Villanueva et al. 2011a) and JFC 103P/Hartley 2 (Mumma et al. 2011). This relatively broad nature includes C<sub>2</sub>H<sub>2</sub>, a nonpolar molecule having a noisier profile than that of either H<sub>2</sub>O or HCN. However, the comeasured continuum profile was also broader in Lcust compared with other panels in Figure 7, suggesting poorer seeing during this observation sequence. This is demonstrated quantitatively by the relatively large Lcust continuum GF ( $1.54 \pm 0.05$ ; see Table 3) compared with continuum GFs from Lp1 on January 13 and February 5 and M2 on February 4, the mean of which is  $1.25 \pm 0.03$ , all three GFs being in agreement within their respective  $1\sigma$  uncertainties.

This makes it difficult to directly compare profile widths in Lcust with those from the three other spectral sequences. We also note that our flux standard (BS4357) spectra were obtained independently of and prior to the comet spectra (e.g., between 11:05 and 11:25 UT, respectively, on February 5). Therefore, the stellar PSFs shown in all panels of Figure 7 should be considered representative only, rather than being reliable indicators of extant conditions during acquisition of the corresponding comet spectra.

Nonetheless, the HCN profile (and perhaps that of C<sub>2</sub>H<sub>2</sub>) exhibited enhanced sunward intensity between  $\rho \sim 300$  and 500 km and a “shoulder” near corresponding distances antisunward. However, such enhanced intensity was not present in the comeasured H<sub>2</sub>O profile. In analogy with CH<sub>3</sub>OH versus nonpolar molecules (C<sub>2</sub>H<sub>6</sub>, CH<sub>4</sub>) encompassed by our January 13 observations, this difference may indicate distinct populations of ices in the nucleus of C/2018 Y1, for

example, if HCN is associated with nonpolar-dominated ice, as noted previously for comets 103P and C/2007 W1. The generally broad nature of HCN (and C<sub>2</sub>H<sub>2</sub>) may reflect the broad comeasured Lcust continuum, which they track in the inner coma to approximately  $\pm 200$ –300 km from the nucleus.

In the Lp1 setting on February 5, both CH<sub>3</sub>OH and OH prompt emission profiles were more extended than those of the nonpolar species, remaining fairly flat within  $\sim 200$  km of the nucleus, then dropping in the sunward direction to closely match those of the other comeasured parent volatiles at larger offset distances. Antisunward, CH<sub>3</sub>OH and OH were considerably more extended, with OH exhibiting pronounced enhancement at  $\rho \sim 500$ –700 km, and with weaker enhancement at corresponding sunward distances. Interestingly, similar enhancements were not seen in the CH<sub>3</sub>OH profile, perhaps indicating the presence of water-rich icy grains at these  $\rho$ -values.

The dust profile was overall stronger antisunward. Most significantly, on January 13, as with C<sub>2</sub>H<sub>6</sub> and CH<sub>4</sub>, it displayed an enhancement that peaked somewhat closer to the nucleus compared with the pronounced CH<sub>3</sub>OH peak near  $\rho = 800$  km as discussed above. We present the possible implications in Section 4.4; however, further detailed quantitative comparison among observed profiles (for all observations), such as potentially one or more compositionally distinct spiraling jets transiting the slit to explain the finer structure in some spatial profiles, is beyond the scope of this study, particularly given the limited nature of our data set on C/2018 Y1.

#### 4.3. Most Complete Sampling of Cometary Methane to Date

We detected 10 distinct rovibrational lines (i.e., excluding individual spin components) of the CH<sub>4</sub>  $\nu_3$  band (Herzberg 1945; see also Section 3 of Gibb et al. 2003) on January 13 and 11 distinct lines on February 5, including emission from the Q branch on both dates (Figure 1). The principal reason for this difference (besides possibly S/N) is that on January 13, the cross-disperser grating set slightly to the red compared to February 5, which, unlike January 13, included order 159 and encompassed the R4 line in both the A and B beams near the blue end of the cropped order (compare Figures 1(a) and (b)). All encompassed CH<sub>4</sub> lines were incorporated into our analysis, with the exception of R2, which, for the geocentric Doppler shift on both dates, was largely obscured by coincident H<sub>2</sub>O absorption to the blue of the corresponding telluric CH<sub>4</sub> line.

Figure 8 illustrates our rotational analysis of CH<sub>4</sub> on February 5. We performed two independent excitation analyses, one based on lower-state rotational energies and the other based on upper-state rotational energies (Figures 8(b) and (c), respectively). The latter are expressed relative to the energy of the lowest rotational level ( $J' = 0$ ) in the upper vibrational state ( $\nu' = 1$ ), corresponding to the upper state of the P1 line transition. The consistent  $T_{\text{rot}}$  from these (within their  $1\sigma$  uncertainties) demonstrates that our retrieval is only weakly sensitive to whether rotational excitation energy is expressed relative to the lowest rotational level in the  $\nu'' = 0$  ( $E_{\text{rot-lower}}$ ) or the  $\nu' = 1$  ( $E_{\text{rot-upper}}$ ) vibrational manifold (see Appendix 5 of Bonev 2005 for details). In both cases, the retrieved  $T_{\text{rot}}$  pertains to the ground vibrational state (through line  $g$  factors; see Equations 1 and 2). For the column sampled by our nucleus-centered spectra, this also reflects the importance of

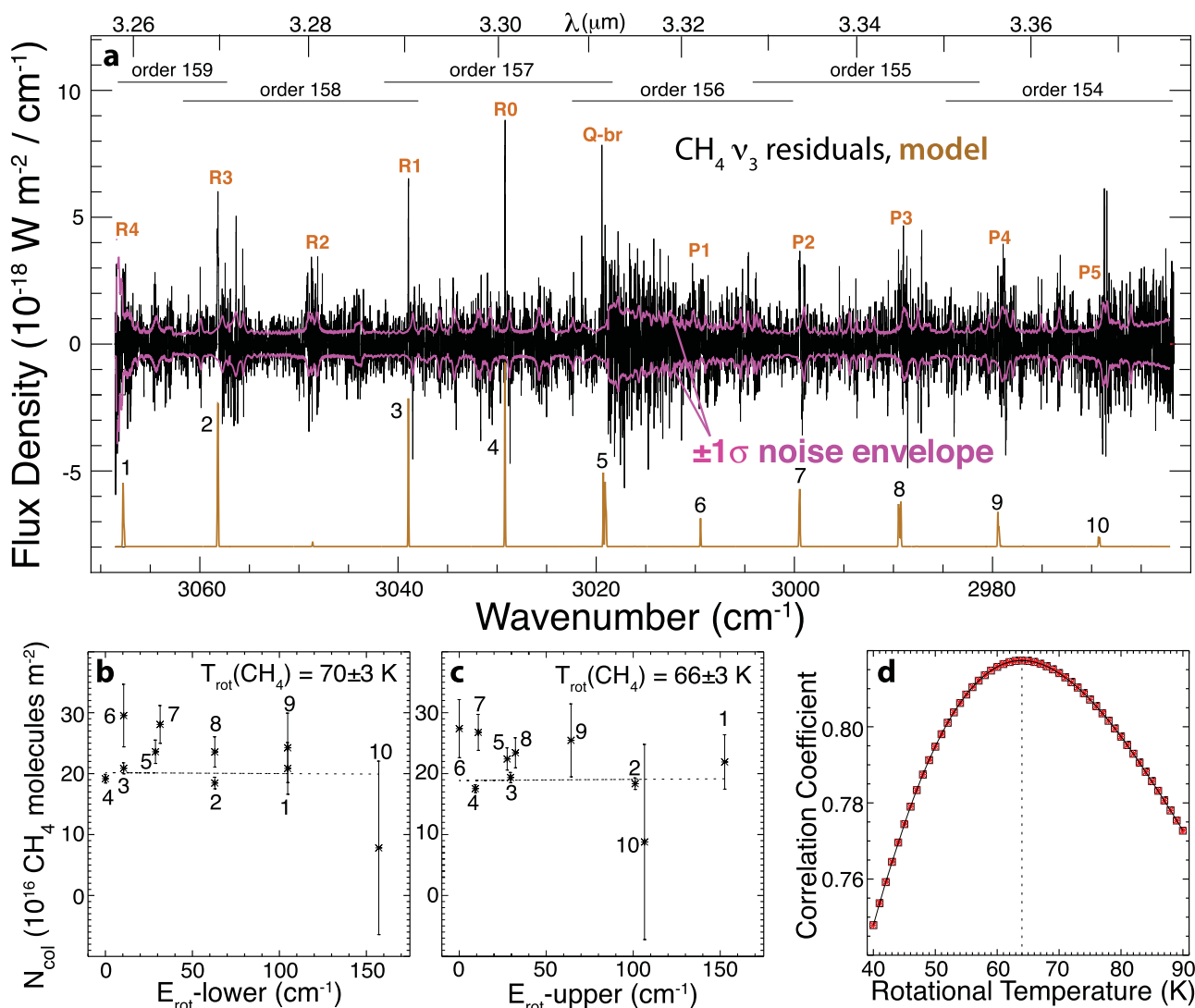


**Figure 8.** (a) Nucleus-centered spectrum of C/2018 Y1 from February 5, representing that shown in Figure 1(b) following subtraction of modeled contributions from all species except CH<sub>4</sub> (including the dust continuum) and below this the best-fit fluorescence model with quantum line designations indicated. (b) and (c) Excitation plots based on lower- and upper-state energies and best-fit  $T_{\text{rot}}$  as discussed in Section 4.3. (d) Correlation between residuals and model as a function of  $T_{\text{rot}}$ .

collisions in thermalizing the coma (see Biver et al. 1999 and DiSanti et al. 2001 for additional discussions).

#### 4.4. Possible Implications of Compositional Results

Compared to the mean abundances measured among comets, our analysis indicates depleted abundances for most molecules, except for “normal” to perhaps even “enriched” C<sub>2</sub>H<sub>6</sub> and enriched CH<sub>3</sub>OH. This is particularly noteworthy given the strongly depleted abundances we measured for CO and C<sub>2</sub>H<sub>2</sub> based on our observations from February 4 and 5, respectively. Our findings may have implications for the processing history of ices prior to their incorporation into the nucleus of C/2018 Y1.

##### 4.4.1. Role of Surface Chemistry on Precometary Carbon-bearing Ices in Determining Composition

Gas-phase (e.g., ion-molecule) formation of C<sub>2</sub>H<sub>6</sub> is energetically inhibited (see, e.g., Herbst et al. 1983; Tielens & Allamandola 1987). Laboratory studies (Stief et al. 1965; Gerakines et al. 1996; Baratta et al. 2002) have provided

evidence for its production through UV photolysis of mixed (H<sub>2</sub>O–CH<sub>4</sub>) or pure CH<sub>4</sub> ice condensed onto interstellar grains. Alternatively, sequential H-atom addition to C<sub>2</sub>H<sub>2</sub> condensed onto grains at the low temperatures (e.g., <30 K) found in the shielded interstellar natal cloud core out of which the solar system formed provides a viable means of producing C<sub>2</sub>H<sub>6</sub> (Tielens 1992). Interstellar grain-surface chemistry was invoked to explain the unexpectedly abundant C<sub>2</sub>H<sub>6</sub> relative to CH<sub>4</sub> first observed in C/1996 B2 (Hyakutake) (Mumma et al. 1996).

Similarly, gas-phase production of methanol is also inhibited; however, surface hydrogenation of condensed CO is efficient at producing a myriad of interstellar molecules, including CH<sub>3</sub>OH (Millar et al. 1991; Charnley et al. 1995; Hudson & Moore 1999). This was demonstrated quantitatively through laboratory yields from proton irradiation of both pure CO and mixed H<sub>2</sub>O–CO ices at low temperatures ( $T \sim 10$ –25 K; Watanabe et al. 2004).

The depleted C<sub>2</sub>H<sub>2</sub> and CO combined with the enriched C<sub>2</sub>H<sub>6</sub> and CH<sub>3</sub>OH measured in C/2018 Y1 could be the result of (i.e., is consistent with) efficient surface chemistry on

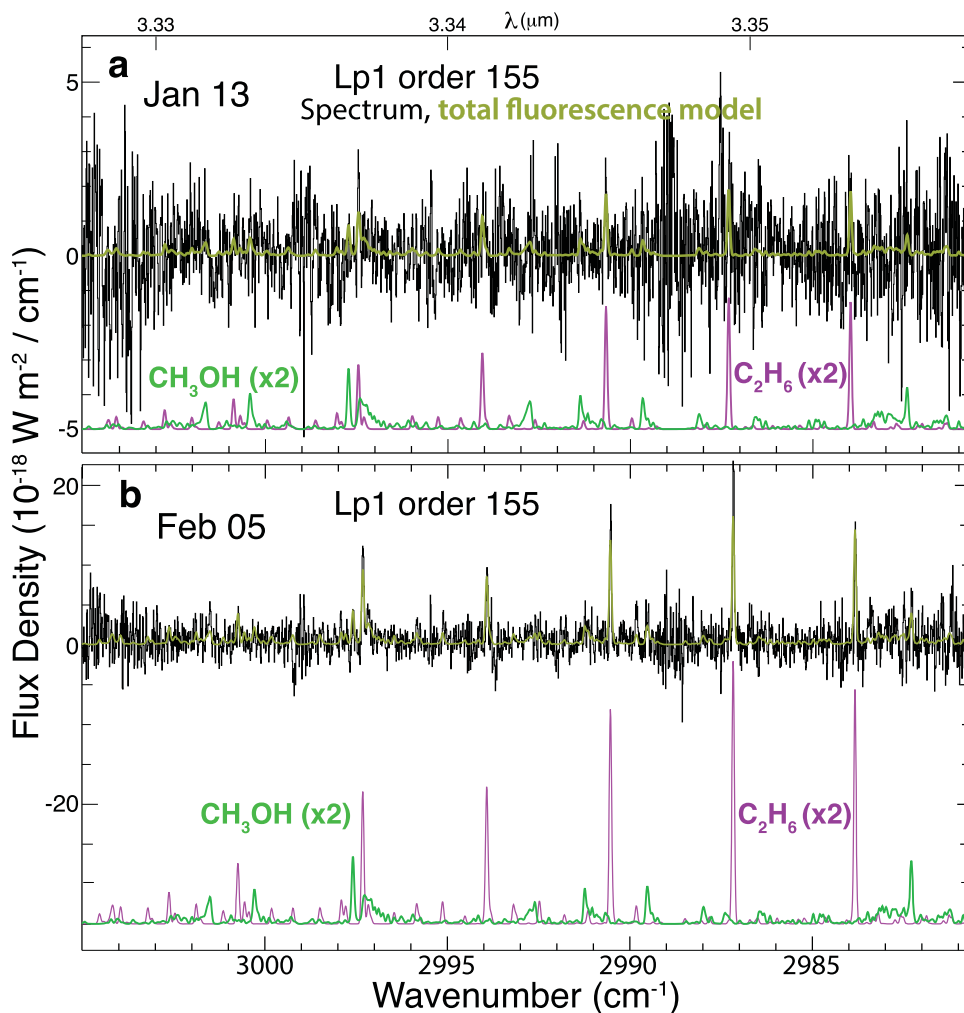


**Figure 9.** Nucleus-centered spectra showing the best order (Lp1/155) for comparing  $C_2H_6$  and  $CH_3OH$  following subtraction of modeled dust,  $CH_4$ , and OH emissions. Each spectrum represents approximately 1 hr on source (Table 1), and the models for  $C_2H_6$  are scaled similarly on the two dates. This demonstrates the substantial difference in  $CH_3OH/C_2H_6$  between our January and February observations (about 24%), while  $CH_4/C_2H_6$  remained constant within the uncertainty. See Figures 5(c) and (d) and discussion in Section 4.4.2.

precometary grains. Assuming the initial amounts of CO and  $C_2H_2$  condensed onto the grain surfaces were similar among ices housed in distinct active regions of the nucleus, a higher efficiency for hydrogenating CO compared with  $C_2H_2$  in the region dominating the activity on January 13 cannot be ruled out (compare  $CH_3OH/C_2H_6$  on January 13 and February 5).

More definitively addressing efficiencies for hydrogenation on interstellar grains would have required obtaining spectra in all three settings (Lp1, M2, and Lcust) on multiple dates. However, as mentioned in Section 2, our emphasis on Comet 46P/Wirtanen—particularly in January but also on February 4—necessarily limited our spectral (and temporal) coverage of C/2018 Y1.

#### 4.4.2. Evidence for and Possible Implications of Compositional Heterogeneity

We obtained spectra in the Lp1 setting on two dates, permitting a comparison of production rates and therefore of relative abundances among measured molecules. Most pronounced was the substantially higher (by 24%) abundance ratio  $CH_3OH/C_2H_6$  on January 13 compared with February 5, while  $CH_4/C_2H_6$  did not change within a  $1\sigma$  uncertainty. This may indicate more polar-rich jet activity on January 13.

This significant change in  $CH_3OH/C_2H_6$  is illustrated in Figure 9, which shows nucleus-centered spectra for the Lp1 order encompassing the largest number of strong  $C_2H_6$  and  $CH_3OH$  lines. We used ratios of  $Q_{nc}$  in establishing abundance ratios for these comensured molecules. We note (Table 3) that the formal GF for  $CH_3OH$  on each date was larger than those for  $CH_4$  or  $C_2H_6$ ; however, especially on February 5, all three GFs agreed within their  $1\sigma$  uncertainties (see below).

A relatively straightforward explanation for this difference in the measured  $CH_3OH/C_2H_6$  is that regions of the nucleus dominating the activity of C/2018 Y1 on January 13 and February 5 differed in their native ice compositions. For example, this could result from differing initial endowments of  $C_2H_2$  and CO condensed onto grain surfaces and/or differing efficiencies for H-atom addition to these reactant molecules in forming  $C_2H_6$  and  $CH_3OH$ , respectively (Section 4.4.1). Either possibility may imply distinct extant conditions among regions in the natal protosolar molecular cloud core and/or the protosolar disk midplane (Willacy et al. 2015; Eistrup et al. 2019).

The change in global abundance ratio  $CH_3OH/C_2H_6$  is reflected in a comparison between the spatial distributions of these two parent volatiles. On January 13 (Figure 7(a)), the



distribution of CH<sub>3</sub>OH was significantly more extended than that of other species, including C<sub>2</sub>H<sub>6</sub>. This difference in spatial profiles suggests an additional outgassing source of methanol, for example, sublimation from polar-rich icy grains in the coma, consistent with its pronounced extension in the projected antisolar direction. On February 5 (Figure 7(d)), when likely (presumably) a different active region dominated the outgassing, the spatial profile of CH<sub>3</sub>OH was significantly less extended and closer to (although still broader than) that of C<sub>2</sub>H<sub>6</sub>, and this is reflected in the lower abundance ratio CH<sub>3</sub>OH/C<sub>2</sub>H<sub>6</sub> on this date.

We note that on January 13, the GF measured for CH<sub>3</sub>OH was significantly larger than that for C<sub>2</sub>H<sub>6</sub>, by  $35\% \pm 5\%$  (Table 3), whereas on February 5, it was only  $\sim 9\%$  larger. Therefore, using the ratios of  $Q_{\text{tot}}$  based on individual GFs suggests an even larger change in CH<sub>3</sub>OH/C<sub>2</sub>H<sub>6</sub> between January 13 and February 5 than that implied by Figure 9, which visually compares only  $Q_{\text{nc}}$ . Also, the spatial inter-relationship between C<sub>2</sub>H<sub>6</sub> and CH<sub>4</sub> was quite similar on January 13 and February 5. Although not identical, their profiles tracked each other much more closely, in contrast to that of CH<sub>3</sub>OH, with evidence provided by the relatively constant abundance ratio CH<sub>4</sub>/C<sub>2</sub>H<sub>6</sub> compared to the substantial change in CH<sub>3</sub>OH/C<sub>2</sub>H<sub>6</sub>, regardless of the value adopted for  $T_{\text{rot}}$  (see Table 4).

#### 4.4.3. Nitrogen Chemistry

With its mean abundance ratio among OCCs approaching 1% relative to H<sub>2</sub>O (Figure 6(h)), NH<sub>3</sub> has traditionally been considered the primary reservoir of volatile nitrogen in most comets. However, reports of ammoniated salts in 67P/Churyumov–Gerasimenko using the VIRTIS-M imaging spectrometer (Poch et al. 2020) and the ROSINA mass spectrometer (Altwegg et al. 2020) during the Rosetta mission suggest a previously unrecognized and potentially substantial reservoir of nitrogen, which has profound implications for both its sequestration and overall abundance in comets. In 67P, NH<sub>3</sub> was measured at an abundance of 0.4% (Läuter et al. 2020), somewhat below its mean among JFCs ( $0.59\% \pm 0.11\%$ ; Dello Russo et al. 2016). Our stringent constraint ( $3\sigma$  upper limit) on the abundance of NH<sub>3</sub> in C/2018 Y1 ( $<0.29\%$  relative to H<sub>2</sub>O; see Tables 3 and 4) implies its less important contribution to the volatile nitrogen inventory when compared with the majority of all comets (both JFCs and OCCs) measured to date.

#### 4.4.4. Placing C/2018 Y1 in Context

##### 4.4.4.1. Comparisons with Contemporaneous Measurements of Water Production in C/2018 Y1

Our study suggests possible short-term variability in  $Q(\text{H}_2\text{O})$ , the value on February 4 being larger than that on February 5 by  $23\% \pm 14\%$  (see Table 4 and Figure 4(b)). However, when comparing with measurements by other observers, whether any (relatively small) differences in  $Q(\text{H}_2\text{O})$  are due to time-variable activity versus, for example, differences in technique or instrument field of view is not clear.

Contemporaneous SOHO-SWAN measurements of the Ly $\alpha$  coma from UT January 13 (M. Combi 2021, personal communication) provide a result that is consistent (within the uncertainties) with our best estimate for  $Q(\text{H}_2\text{O})$  ( $179 \pm 18 \times 10^{26} \text{ s}^{-1}$ ). Given the much larger spatial coverage of SOHO,

this suggests that most of the H<sub>2</sub>O in C/2018 Y1 was released within  $\sim 2000$  km of the nucleus (corresponding to the spatial coverage of our observations; Figure 7(a)). Also, the mean of our water production rates from January 13 and February 4–5 ( $196 \pm 12 \times 10^{26} \text{ s}^{-1}$ ) is only somewhat larger than the value from optical observations of C/2018 Y1 with TRAPPIST on UT 2019 January 29 ( $168 \pm 5 \times 10^{26} \text{ s}^{-1}$ ; Moulane et al. 2020).

##### 4.4.4.2. Assessing Parent–Product Relationships in C/2018 Y1

Comparing the measured production rates of product species with those of potential parent molecules can provide insight as to their sources (specifically, CN versus HCN, C<sub>2</sub> versus C<sub>2</sub>H<sub>2</sub>, NH<sub>2</sub> versus NH<sub>3</sub>). In the case of C/2018 Y1, our results, together with those from TRAPPIST (E. Jehin & Y. Moulane 2021, private communication), permit such comparisons. On 2019 February 9 (the date closest to our February 5 observations), TRAPPIST observed the abundance ratios CN/OH, C<sub>2</sub>/CN, and NH/OH to be within the “typical” range (in the case of NH/OH, perhaps somewhat enriched). This suggests that HCN is plausibly the sole source of CN, whereas C<sub>2</sub>H<sub>2</sub> cannot account for the measured C<sub>2</sub> (by a factor of almost 3), nor can NH<sub>3</sub> account for the measured NH (by a factor of almost 2). Based on these last two comparisons, one or more additional progenitors are required to account for both the C<sub>2</sub> and NH abundances measured in C/2018 Y1; however, since photodissociation of NH<sub>3</sub> proceeds through NH<sub>2</sub> (not reported here), a quantitative comparison of NH<sub>3</sub> with NH is clearly less meaningful.

##### 4.4.4.3. Compositional Comparisons with Other Comets

The abundance we find for C<sub>2</sub>H<sub>2</sub> in C/2018 Y1 (0.082% with respect to H<sub>2</sub>O; Table 4) is well below its mean among OCCs ( $0.16\% \pm 0.03\%$ ) but consistent with its mean among JFCs ( $0.07\% \pm 0.02\%$ ; Dello Russo et al. 2016). It is somewhat higher than that measured in JFCs 73P/Schwassmann–Wachmann 3 ( $\sim 0.04\%$ , representing the average of fragments B and C; Dello Russo et al. 2007) and 21P/Giacobini–Zinner, in which a  $3\sigma$  upper limit as low as 0.02% was reported from iSHELL observations during its 2018 apparition (Faggi et al. 2019). Both 73P and 21P are members of the carbon chain–depleted population of comets (A’Hearn et al. 1995; Fink 2009; Cochran et al. 2012), as defined by the abundance ratio C<sub>2</sub>/CN (see Table 4 of A’Hearn et al. 1995).

In spite of this, classifying C/2018 Y1 in terms of its depleted C<sub>2</sub>H<sub>2</sub> alone does not provide adequate context regarding its place within the taxonomy of comets based on parent volatile compositions. Most notably, its C<sub>2</sub>H<sub>6</sub> abundance is in agreement with (or slightly larger than) the mean value among OCCs ( $0.63\% \pm 0.10\%$  relative to H<sub>2</sub>O; Dello Russo et al. 2016), whereas C<sub>2</sub>H<sub>6</sub> is much less abundant in both 73P ( $\sim 0.1\%$ ; Dello Russo et al. 2007) and 21P ( $\sim 0.1\%–0.3\%$ ; Mumma et al. 2000; DiSanti et al. 2013; Faggi et al. 2019; Roth et al. 2020). Similarly, CH<sub>3</sub>OH is enriched in C/2018 Y1; however, it is strongly depleted in 73P (Dello Russo et al. 2007). In terms of its CH<sub>4</sub>, C<sub>2</sub>H<sub>6</sub>, CH<sub>3</sub>OH, and CO, C/2018 Y1 appears similar to C/2004 M4 (SWAN), yet C<sub>2</sub>H<sub>2</sub> was not measured for that OCC (DiSanti et al. 2009). The point is that to place C/2018 Y1 (or any comet) within the still-evolving compositional taxonomy requires examining the full suite of

measured parent volatiles, with each newly measured comet having the potential to provide additional insights.

## 5. Summary

We obtained high-resolution preperihelion spectra of long-period comet C/2018 Y1 using iSHELL, the powerful cross-dispersed high-resolution facility IR spectrograph at the IRTF, on three UT dates, 2019 January 13 and February 4–5. We report production rates for H<sub>2</sub>O and eight trace volatiles (CO, H<sub>2</sub>CO, CH<sub>3</sub>OH, CH<sub>4</sub>, C<sub>2</sub>H<sub>2</sub>, C<sub>2</sub>H<sub>6</sub>, HCN, and NH<sub>3</sub>) and abundance ratios for all volatiles relative to both C<sub>2</sub>H<sub>6</sub> and H<sub>2</sub>O. Our study revealed that C<sub>2</sub>H<sub>6</sub> and CH<sub>3</sub>OH were consistent with or somewhat enriched compared to their respective mean abundances (with respect to H<sub>2</sub>O) found among such comets from the Oort cloud, while all other species were depleted relative to their respective mean abundances.










Several important conclusions are revealed by our study of C/2018 Y1.

1. *Advancing sensitivity limits.* Compared to its predecessor instrument, iSHELL improves sensitivity by a factor of at least 5 (Section 4.1). This extends the ability to measure molecular production rates and also reliable spatial profiles of emission to weaker comets, thereby opening a new realm in studies of cometary parent volatile compositions. With its cross-dispersed capability and active IR guiding, iSHELL permits comparing coma abundances for and outflow of multiple molecules and dust in comets having an FoM as low as  $\sim 0.1$  (Figure 7(a)).
2. *Potentially distinct sources of volatile release.* Overall, our spatial profiles of volatile emission (Figure 7) are broader and more complex for polar molecules (H<sub>2</sub>O, CH<sub>3</sub>OH) than for nonpolar (C<sub>2</sub>H<sub>6</sub>, CH<sub>4</sub>) or weakly polar (CO) molecules (Section 4.2). This suggests that distinct sources are responsible for their release, perhaps indicating polar- versus nonpolar-dominated associations of ice in the nucleus of C/2018 Y1.
3. *Nearly complete measure of CH<sub>4</sub>.* The continuous spectral coverage of iSHELL in the 3.3  $\mu\text{m}$  region, together with the unusually large geocentric Doppler shift, allowed simultaneously measuring many distinct rovibrational lines of CH<sub>4</sub> in C/2018 Y1 on two dates. This represents the most complete characterization of CH<sub>4</sub> in any comet measured to date (Figures 1 and 8 and Section 4.3).
4. *Evidence for compositional heterogeneity.* A decisively lower abundance ratio CH<sub>3</sub>OH/C<sub>2</sub>H<sub>6</sub> was measured on UT 2019 February 5 compared with January 13, while CH<sub>4</sub>/C<sub>2</sub>H<sub>6</sub> agreed within the uncertainty. This suggests a degree of inhomogeneity in the composition of ice in the nucleus of C/2018 Y1 (Figure 9 and Sections 4.2 and 4.4). The intensity enhancements observed in the spatial profiles (in particular, for H<sub>2</sub>O and CH<sub>3</sub>OH) could also indicate heterogeneity, or at least very dynamic and variable outgassing behavior.

Our study of C/2018 Y1 bodes well for future studies of cometary parent volatile compositions. The ability to extend this type of study to comets with  $Q(\text{H}_2\text{O})$  around  $10^{28}$  molecules  $\text{s}^{-1}$  (as was the case with C/2018 Y1) coupled with the flexible scheduling afforded by the IRTF (including daytime observing capability, which is unique among ground-based IR platforms) increases the number of accessible targets by a considerable amount.

This work is supported through the NASA Planetary Astronomy/Solar System Observations Program (grants 18-SSO18\_2-0040, 80NSSC17K0705, NNX12AG24G), the Planetary Atmospheres/Solar System Workings Program (grants 80NSSC20K0651, NNX17AC86G), the Emerging Worlds Program (grant 80NSSC20K0341), the National Science Foundation (grants AST-2009398, AST-1616306, AST-1615441), and the NASA Earth and Space Science Fellowship Program (NNX16AP49H). Support is acknowledged by the NASA Astrobiology Institute through funding awarded to the Goddard Center for Astrobiology under proposal 13-13NAI7\_0032. We thank the two anonymous reviewers who provided constructive comments that improved the paper. M.A.D. thanks M. Combi for providing unpublished water production rates for C/2018 Y1 from SOHO-SWAN observations, and E. Jehin and Y. Moulane for providing unpublished production rates for C/2018 Y1 product species from TRAPPIST observations. We also thank the staff of the IRTF, noting that the data presented herein were obtained at the NASA Infrared Telescope Facility, operated by the University of Hawai'i under contract NN14CK55B with the National Aeronautics and Space Administration. We are most fortunate to have the opportunity to conduct observations from Maunakea, recognizing the very significant cultural role and reverence that it continues to have within the indigenous Hawaiian community.

## ORCID iDs

Michael A. DiSanti  <https://orcid.org/0000-0001-8843-7511>  
 Boncho P. Bonev  <https://orcid.org/0000-0002-6391-4817>  
 Neil Dello Russo  <https://orcid.org/0000-0002-8379-7304>  
 Adam J. McKay  <https://orcid.org/0000-0002-0622-2400>  
 Nathan X. Roth  <https://orcid.org/0000-0002-6006-9574>  
 Mohammad Saki  <https://orcid.org/0000-0003-2277-6232>  
 Erika L. Gibb  <https://orcid.org/0000-0003-0142-5265>  
 Ronald J. Vervack Jr.  <https://orcid.org/0000-0002-8227-9564>  
 Younas Khan  <https://orcid.org/0000-0003-4773-2674>

## References

- A'Heam, M. F., Millis, R. L., Schleicher, D. G., Osip, D. J., & Birch, P. V. 1995, *Icar*, **118**, 223
- Altwegg, K., Balsiger, H., Hänni, N., et al. 2020, *NatAs*, **4**, 533
- Baratta, G. A., Leto, G., & Palumbo, M. E. 2002, *A&A*, **384**, 343
- Biver, N., Bockelee-Morvan, D., Crovisier, J., et al. 1999, *AJ*, **118**, 1850
- Bockelee-Morvan, D., & Biver, N. 2017, *RSPTA*, **375**, 20160252
- Bockelee-Morvan, D., Crovisier, J., Mumma, M. J., & Weaver, H. A. 2004, in *Comets II*, ed. M. C. Festou, H. U. Keller, & H. A. Weaver (Tucson, AZ: Univ. Arizona Press), 391
- Bonev, B. P. 2005, PhD thesis, Univ. Toledo
- Bonev, B. P., Dello Russo, N., DiSanti, M. A., et al. 2021, *PSJ*, **2**, 45
- Bonev, B. P., Mumma, M. J., DiSanti, M. A., et al. 2006, *ApJ*, **653**, 774
- Charnley, S. B., Kress, M. E., Tielens, A. G. G. M., & Millar, T. J. 1995, *ApJ*, **448**, 232
- Cochran, A. L., Barker, E. S., & Gray, C. L. 2012, *Icar*, **218**, 144
- Collins, W. D., Lee-Taylor, J. M., Edwards, D. P., & Francis, G. L. 2006, *JGR*, **111**, D18109
- Combes, M., Moroz, V. I., Crovisier, J., et al. 1988, *Icar*, **76**, 404
- Dello Russo, N., DiSanti, M. A., Magee-Sauer, K., et al. 2004, *Icar*, **168**, 186
- Dello Russo, N., DiSanti, M. A., Mumma, M. J., Magee-Sauer, K., & Rettig, T. W. 1998, *Icar*, **135**, 377
- Dello Russo, N., Kawakita, H., Vervack, R. J., Jr., & Weaver, H. A. 2016, *Icar*, **278**, 301
- Dello Russo, N., Vervack, R. J., Jr., Weaver, H. A., et al. 2007, *Natur*, **448**, 172
- DiSanti, M. A., Bonev, B. P., Dello Russo, N., et al. 2017, *AJ*, **154**, 246
- DiSanti, M. A., Bonev, B. P., Gibb, E. L., et al. 2016, *ApJ*, **820**, 34
- DiSanti, M. A., Bonev, B. P., Gibb, E. L., et al. 2018, *AJ*, **156**, 258

- DiSanti, M. A., Bonev, B. P., Magee-Sauer, K., et al. 2006, *ApJ*, **650**, 470
- DiSanti, M. A., Bonev, B. P., Villanueva, G. L., & Mumma, M. J. 2013, *ApJ*, **763**, 1
- DiSanti, M. A., Mumma, M. J., Dello Russo, N., & Magee-Sauer, K. 2001, *Icar*, **153**, 361
- DiSanti, M. A., Villanueva, G. L., Milam, S. N., et al. 2009, *Icar*, **203**, 589
- Eistrup, C., Walsh, C., & van Dishoeck, E. F. 2019, *A&A*, **629**, A84
- Faggi, S., Mumma, M. J., Villanueva, G. L., Paganini, L., & Lippi, M. 2019, *AJ*, **158**, 254
- Faggi, S., Villanueva, G. L., Mumma, M. J., & Paganini, L. 2018, *AJ*, **156**, 68
- Fink, U. 2009, *Icar*, **201**, 311
- Gerakines, P. A., Schutte, W. A., & Ehrenfreund, P. 1996, *A&A*, **312**, 289
- Gibb, E. L., Bonev, B. P., Villanueva, G. L., et al. 2012, *ApJ*, **750**, 102
- Gibb, E. L., Mumma, M. J., Dello Russo, N., DiSanti, M. A., & Magee-Sauer, K. 2003, *Icar*, **165**, 391
- Herbst, E., Adams, N. G., & Smith, D. 1983, *ApJ*, **269**, 329
- Herzberg, G. 1945, *Molecular Spectra and Molecular Structure II. Infrared and Raman Spectra of Polyatomic Molecules* (New York: Van Nostrand)
- Hoban, S. M., Mumma, M. J., Reuter, D. C., et al. 1991, *Icar*, **93**, 122
- Hudson, R. L., & Moore, M. H. 1999, *Icar*, **140**, 451
- Langevin, Y., Kissel, J., Bertaux, J.-L., & Chassefiere, E. 1988, *A&A*, **187**, 761
- Langland-Shula, L. E., & Smith, G. H. 2011, *Icar*, **213**, 280
- Läuter, M., Kramer, T., Rubin, M., & Altwegg, K. 2020, *MNRAS*, **498**, 3995
- Lippi, M., Villanueva, G. L., DiSanti, M. A., et al. 2013, *A&A*, **551**, A51
- Martin, E. C., Fitzgerald, M. P., McLean, I. S., et al. 2018, *Proc. SPIE*, **10702**, 107020A
- Millar, T. J., Herbst, E., & Charnley, S. B. 1991, *ApJ*, **369**, 147
- Moroz, V. I., Combes, M., Bibring, J. P., et al. 1987, *A&A*, **187**, 513
- Morse, A. D., & Chan, Q. H. S. 2019, *ESC*, **3**, 1773
- Moulane, Y., Jehin, E., Pozuelos, F. J., et al. 2020, *EPSC*, **14**, 419
- Mumma, M. J., Bonev, B. P., Villanueva, G. L., et al. 2011, *ApJL*, **734**, L7
- Mumma, M. J., & Charnley, S. B. 2011, *ARA&A*, **49**, 471
- Mumma, M. J., DiSanti, M. A., Dello Russo, N., et al. 1996, *Sci*, **271**, 1310
- Mumma, M. J., DiSanti, M. A., Dello Russo, N., et al. 2003, *AdSpR*, **31**, 2563
- Mumma, M. J., DiSanti, M. A., Dello Russo, N., Magee-Sauer, K., & Rettig, T. W. 2000, *ApJL*, **531**, L155
- Paganini, L., Camarca, M. N., Mumma, M. J., et al. 2019, *AJ*, **158**, 98
- Paganini, L., Mumma, M. J., Boehnhardt, H., et al. 2013, *ApJ*, **766**, 100
- Poch, O., Istiqomah, I., Quirico, E., et al. 2020, *Sci*, **367**, aaw7462
- Radeva, Y. L., Mumma, M. J., Bonev, B. P., DiSanti, M. A., & Villanueva, G. L. 2010, *Icar*, **206**, 764
- Rayner, J., Tokunaga, A., Jaffe, D., et al. 2016, *Proc. SPIE*, **9908**, 990884
- Roth, N. X., Gibb, E. L., Bonev, B. P., et al. 2018, *AJ*, **156**, 251
- Roth, N. X., Gibb, E. L., Bonev, B. P., et al. 2020, *AJ*, **159**, 42
- Schleicher, D. G., & Bair, A. 2014, in *Proc. Asteroids Comets Meteors Conf.*, ed. K. Muinonen et al. (Helsinki: Univ. Helsinki), 496
- Scoles, S. 2019, *Sci*, **364**, 818
- Stief, L. J., DeCarlo, V. J., & Hillman, J. J. 1965, *JChPh*, **43**, 2490
- Tielens, A. G. G. M. 1992, in *Chemistry and Spectroscopy of Interstellar Molecules*, ed. K. K. Bohme (Tokyo: Univ. Tokyo Press), 237
- Tielens, A. G. G. M., & Allamandola, L. J. 1987, in *Physical Processes in Interstellar Clouds*, ed. G. E. Morfill & M. Scholer (Dordrecht: Reidel), 333
- Tokunaga, A. T., Toomey, D. W., Carr, J., Hall, D. N., & Epps, H. W. 1990, *Proc. SPIE*, **1235**, 131
- Villanueva, G. L., DiSanti, M. A., Mumma, M. J., & Xu, L.-H. 2012a, *ApJ*, **747**, 37
- Villanueva, G. L., Magee-Sauer, K., & Mumma, M. J. 2013, *JQSRT*, **129**, 158
- Villanueva, G. L., Mumma, M. J., Bonev, B. P., et al. 2009, *ApJL*, **690**, L5
- Villanueva, G. L., Mumma, M. J., Bonev, B. P., et al. 2012b, *JQSRT*, **113**, 202
- Villanueva, G. L., Mumma, M. J., DiSanti, M. A., Bonev, B. P., & Gibb, E. L. 2011a, *Icar*, **216**, 227
- Villanueva, G. L., Mumma, M. J., & Magee-Sauer, K. 2011b, *JGRE*, **116**, E08012
- Villanueva, G. L., Mumma, M. J., Novak, R. E., & Hewagama, T. 2008, *JQSRT*, **109**, 883
- Watanabe, N., Nagaoka, A., Shiraki, T., & Kouchi, A. 2004, *ApJ*, **616**, 638
- Weaver, H. A., Feldman, P. D., A'Hearn, M. F., Dello Russo, N., & Stern, S. A. 2011, *ApJL*, **734**, L5
- Willacy, K., Alexander, C., Ali-Dib, M., et al. 2015, *SSRv*, **197**, 151
- Xie, X., & Mumma, M. J. 1996, *ApJ*, **464**, 442